

MEASUREMENT OF EXCITATION ENERGY OF NEUTRON-RICH PRECURSOR
FRAGMENTS

by

Michelle Anthea Mosby

A DISSERTATION

Submitted to
Michigan State University
in partial fulfillment of the requirements
for the degree of

Chemistry – Doctor of Philosophy

2014

ABSTRACT

MEASUREMENT OF EXCITATION ENERGY OF NEUTRON-RICH PRECURSOR FRAGMENTS

by

Michelle Anthea Mosby

Projectile fragmentation forms the basis for beam production at radioactive beam facilities such as the National Superconducting Cyclotron Laboratory (NSCL), yet uncertainties remain about the specifics of the production mechanism. For example, very little is known about the excitation energy of the precursors of the observed final fragments. In the present work, isotopes of sodium, neon, and fluorine produced in the fragmentation of a ^{32}Mg beam at 86 MeV/nucleon in a beryllium target, ranging in mass loss from $\Delta A = 3-12$, were observed and the coincident neutrons were detected using the Modular Neutron Array (MoNA). Neutron hit multiplicity in MoNA was compared to output from the statistical evaporation model PACE which was passed through a GEANT4 simulation to account for detector response with a χ^2_ν analysis. The neutron hit multiplicity distributions were used to determine the mass loss and excitation energy of the precursor fragments created in the fast step of the reaction. The mass loss and excitation energy were compared to abrasion/ablation models and an internuclear cascade model, ISABEL. For sodium and neon observed fragments, a single precursor mass was found, with a wide range of high excitation energies, up to 60 MeV. Observed fluorine isotopes were also found to have high excitation energies, ranging from 40-80 MeV, but with some variation in precursor mass.

ACKNOWLEDGMENTS

I would like to thank Dave Morrissey for serving as my advisor. He took me on as a student in unconventional circumstances, and helped me begin a new project quickly. He was always willing to answer questions, but pushed me to think independently about my research. I would also like to thank the members of my committee, Paul Mantica, Michael Thoennesen, and Artemis Spyrou, for their time and dedication to my project. I would especially like to thank Michael Thoennesen for his expertise with MoNA.

I would like to thank the entire MoNA collaboration. Without them, I wouldn't have had a detector on which to run my experiment or people to sit the many shifts. I would especially like to thank the MoNA graduate students (Greg Christian, Shea Mosby, Jesse Snyder, and Jenna Smith) for allowing me to become an unofficial part of your group. Your expertise was invaluable to completing my thesis project. I would also like to thank all of my fellow graduate students. You were always there for a coding tip, a laugh, a cup of coffee, or a beer after a very long week.

A great deal of thanks is also owed to my parents. They supported me throughout the whole process, even the unconventional end. For their supportive phone calls and hours of watching squirrely babies while I typed away on the computer, I am forever grateful.

And most importantly, I thank my husband, Shea. You were there for every step of this journey, always offering your support. There is no way I would have achieved this without you. There are simply no words to adequately describe my gratitude. Thank you.

TABLE OF CONTENTS

LIST OF TABLES	vi
LIST OF FIGURES	vii
CHAPTER 1 INTRODUCTION	1
CHAPTER 2 FRAGMENTATION REACTIONS	5
2.1 Abrasion/ablation model	5
2.1.1 Excitation energy generation in the abrasion/ablation framework	6
2.1.2 Macroscopic excitation model	6
2.1.3 Microscopic excitation model	9
2.2 Internuclear cascade model	11
2.3 De-excitation of prefragments	15
CHAPTER 3 EXPERIMENTAL DETAILS	18
3.1 Beam characteristics	18
3.1.1 Primary beam	18
3.1.2 Secondary beam	18
3.2 Experimental Configuration	19
3.2.1 Beam line detectors	21
3.2.1.1 A1900 focal plane scintillator	21
3.2.1.2 Tracking Cathode Readout Drift Chambers	22
3.2.2 Target chamber	23
3.2.3 Sweeper magnet	23
3.2.4 Focal plane detectors	24
3.2.5 Modular Neutron Array	25
3.2.6 Electronics and Data acquisition	26
CHAPTER 4 ANALYSIS	29
4.1 Overview	29
4.2 Calibrations	29
4.2.1 Neutron detectors: MoNA/MoNA'	29
4.2.2 Charged particle detectors	32
4.2.2.1 Cathode readout drift chambers	32
4.2.2.2 Scintillators	32
4.2.2.3 Ion chamber	33
4.3 Charged fragment identification	34
4.3.1 ^{32}Mg beam selection	34
4.3.2 Element identification	35
4.3.3 Isotope separation	36
4.4 Fragment production cross section	40

4.5	Neutron hits	42
CHAPTER 5	RESULTS	45
5.1	Detector modelling	45
5.2	Neutron evaporation simulation	46
5.3	Reaction precursor fragments	51
CHAPTER 6	COMPARISON TO REACTION MODEL	57
CHAPTER 7	CONCLUSIONS	61
BIBLIOGRAPHY	63

LIST OF TABLES

Table 2.1	Input variables for calculating the fraction of energy equilibrated during the abrasion process expressed in Equation 2.18.	11
Table 2.2	Sample input file for PACE calculation	16
Table 3.1	Logic signals sent between the Sweeper and MoNA/MoNA' subsystems. Valid time signals must surpass the CFD threshold	27
Table 4.1	Correction parameters for the thin scintillator and ion chamber positions .	34
Table 4.2	Tabulation of the calculated mass-to-charge ratios, velocity of beam fragments, and time-of-flight from A1900 to the timing scintillator for the secondary beam, ^{32}Mg , and the major contaminants.	35
Table 4.3	Time-of-flight correction parameters for the 3.15 Tm setting. Polynomial order was determined empirically.	42
Table 4.4	Time-of-flight correction parameters for the 3.75 Tm setting	42
Table 4.5	Time-of-flight correction parameters for the 2.97 Tm setting	42
Table 4.6	Comparison of observed experimental production cross sections for centered charged fragments with LISE++ predictions	43

LIST OF FIGURES

Figure 1.1	Chart of the nuclides with stable nuclei shown as black squares [8]	2
Figure 1.2	Schematic representation of a projectile fragmentation reaction in the two-step abrasion/ablation model	3
Figure 2.1	Excitation energy (E^*) versus abrasion mass loss ($\Delta A_{\text{abr}} = A_b - A_f^*$) for a macroscopic (Wilson [24]) and a microscopic (Gaimard [25]) abrasion model.	12
Figure 2.2	Excitation energy (E^*) versus abrasion mass loss ($\Delta A_{\text{abr}} = A_i - A^*$) for a macroscopic model (Wilson [24]), a microscopic model (Gaimard [25]) and an INC calculation (ISABEL [27], [26]) for the reaction of ^{32}Mg with Be. ISABEL line represents the average E^* found for fragments with $Z=11$. The bounds of the ISABEL region are given by the RMS of the excitation energy distribution for each $A_b - A_f^*$, see the text.	14
Figure 2.3	Schematic view of the evaporation of neutrons from the excited pre-fragment as an isotropic process in the rest, when angular momentum is not important. However, due to the high forward momentum of the prefragment in the lab frame, the evaporated neutrons become highly forward focused.	17
Figure 3.1	Schematic view of the Sweeper-MoNA experimental setup in the N2 vault at NSCL.	20
Figure 3.2	Schematic view of the charged particle detectors near the target and at the focal plane of the Sweeper magnet	20
Figure 3.3	Schematic view of the operation of a CRDC from Ref. [33].	22
Figure 3.4	Calculated central values of the rigidities of the fragments in the focal plane of the Sweeper magnet for each of the three $B\rho$ settings used in the experiment. The settings are distinguished by the magnet current in amperes.	24
Figure 3.5	A schematic diagram of the combinations of the timing signals for the MoNA/MoNA' and Sweeper electronics used to form the Level 1 and Level 2 triggers.	28

Figure 4.1	Schematic representation of an air shower resulting from the interaction of a high-energy cosmic ray, in this case a proton, with the atmosphere [39]. The scattering and decay angles are greatly exaggerated.	30
Figure 4.2	Typical mask images obtained for calibration are show for the two cathode readout drift chambers (CRDCs) located after the Sweeper magnet. The holes in the mask were used to determine the slopes and offsets for the position calibration. A ^{28}Mg beam was used for these mask calibrations.	32
Figure 4.3	Beam identification plots using charge deposited in the scinillator upstream of the target versus ToF from the A1900 object plane to the timing scintillator in the vault.	36
Figure 4.4	Energy loss signals from the ion chamber as a function of the ToF from the scinillator upstream of the target to the thin scintillator downstream of the Sweeper magnet. Elemental separation is shown for the three Sweeper rigidity settings used in this work: (a) 2.97 Tm, (b) 3.15 Tm, (c) 3.45 Tm.	37
Figure 4.5	3-d histogram of x-position vs x-angle vs time-of-flight observed for Ne isotopes with the 3.15 Tm setting of the Sweeper magnet.	38
Figure 4.6	Projection of the time-of-flight shown in Figure 4.5 onto the x-position vs. x-angle plane. Colors represent the time-of-flight. Bands of constant color were used to construct a corrected time-of-flight parameter	39
Figure 4.7	“Emittance” versus corrected time of flight for the neon data obtained with the 3.15 Tm magnet setting, resulting from the projection of the data shown in Figure 4.6	40
Figure 4.8	Particle identification functions for the observed isotopes for sodium (4.8a), neon (4.8b), and fluorine (4.8c) from the 2.97 Tm setting, sodium (4.8d), neon (4.8e), and fluorine (4.8f) from the 3.15 Tm setting, and neon (4.8g) from the 3.75 Tm setting.	41
Figure 4.9	Neutron kinetic energy from MoNA/MoNA' for a ^{25}Ne final fragment.	44
Figure 5.1	Neutron hit multiplicity data for the observed sodium fragments (^{29}Na (5.1a) - ^{25}Na (5.1e))	47
Figure 5.2	Neutron hit multiplicity data for the observed neon fragments (^{29}Ne (5.2a) - ^{24}Ne (5.2f))	48
Figure 5.3	Neutron hit multiplicity data for the observed fluorine fragments (^{23}F (5.3a) - ^{21}F (5.3c))	49

Figure 5.4	Comparison of the experimental hit multiplicity with the results of the PACE/GEANT4 simulation for ^{25}Ne final fragments. The hit multiplicity distributions from the assumed ^{30}Ne , ^{29}Ne , and ^{28}Ne prefragments at the “best” excitation energies of 43, 23, and 14 MeV respectively, are shown.	50
Figure 5.5	The reduced χ^2_{ν} surface obtained for the observed sodium fragments, see the text for an explanation. Observed fragments were 5.5a ^{29}Na , 5.5b ^{28}Na , 5.5c ^{27}Na , 5.5d ^{26}Na , and 5.5e ^{25}Na	52
Figure 5.6	The reduced χ^2_{ν} surface obtained for the observed neon fragments, see the text for an explanation. Observed fragments were 5.6a ^{29}Ne , 5.6b ^{28}Ne , 5.6c ^{27}Ne , 5.6d ^{26}Ne , and 5.6e ^{25}Ne	53
Figure 5.7	The reduced χ^2_{ν} surface obtained for the observed fluorine fragments, see the text for an explanation. Observed fragments were 5.7a ^{23}F , 5.7b ^{22}F , and 5.7c ^{21}F	54
Figure 5.8	Excitation energy (E^*) obtained from the χ^2_{ν} analysis versus total mass loss ($\Delta A = A_i - A_f$) for the observed isotopes with linear fits to the data.	55
Figure 5.9	Excitation energy (E^*) versus mass loss in the fast reaction step ($A_b - A_f^*$). Two points (connected by a dashed line) are shown for each observed fluorine isotope, as the difference between χ^2_{ν} minima for the simulated prefragments is small.	56
Figure 6.1	Excitation energy (E^*) versus mass loss in the fast reaction step ($A_b - A_f^*$). Two abrasion/ablation models are shown: Wilson [24] and Gaimard [25]. An internuclear cascade model is also shown, ISABEL [26], [27]. The line represents the average excitation energy produced in the simulation for a precursor fragment with charge $Z=11$. The bounds of the ISABEL region give the RMS for the excitation energy distribution for a given mass loss, again for $Z=11$. The trends are similar for lower charges.	58
Figure 6.2	Excitation energy (E^*) distributions for $Z=11$ (Na) precursor fragments from the ISABEL model of the present reaction ($^{32}\text{Mg} + ^9\text{Be}$). Sodium fragments are shown to illustrate a fast-step mass loss of one.	59
Figure 6.3	Contours of the relative production cross section for precursor fragments from the ISABEL model of the reaction of ^{32}Mg with ^9Be	60
Figure 6.4	Normalized production cross section for sodium ($Z^*=11$) precursor fragments from the ISABEL model of the reaction of ^{32}Mg with ^9Be	60

Chapter 1

INTRODUCTION

The nuclear landscape, shown for example in Figure 1.1, consists of a relatively few stable nuclei and a far greater number of nuclei which decay. The more exotic regions, farther from the so-called valley of stability, are characterized by very short half-lives, of order a few hundred milliseconds or less. The technique called projectile fragmentation was developed to produce and study exotic nuclei with short half lives. This method allows for the rapid production and physical separation of exotic nuclei, allowing their properties to be studied before decay. Projectile fragmentation is currently the method of choice to produce nuclei far from stability, such as those along the proton and particularly near the neutron drip-lines [1].

Projectile fragmentation forms the basis for many radioactive beam facilities, but the mechanism is not well understood, particularly for the production of neutron-rich nuclei. Measurements of the production cross sections for final fragments are extensive [2], [3], [4], [5] and have been empirically modelled in programs such as LISE++ [6] using the formula EPAX [7]. Such knowledge of the cross sections in projectile fragmentation allows the reaction to be used reliably for beam production.

Many methods exist to study the mechanism of the reaction, however, these studies have only concentrated on the properties of the final observed fragments. Studies of the parallel momentum distributions [9], [10], [11], [12] have shown that relatively simple descriptions, using the mass numbers of the projectile and final fragment as parameters, can characterize the widths of the distributions, without detailed consideration of the reaction intermediates. Similar relationships have been developed to describe the widths of the perpendicular momentum distributions, where the expression was modified by the addition of a Coulomb kick to the fragment [11].

The projectile fragmentation reaction has been described as a two-step process, and until

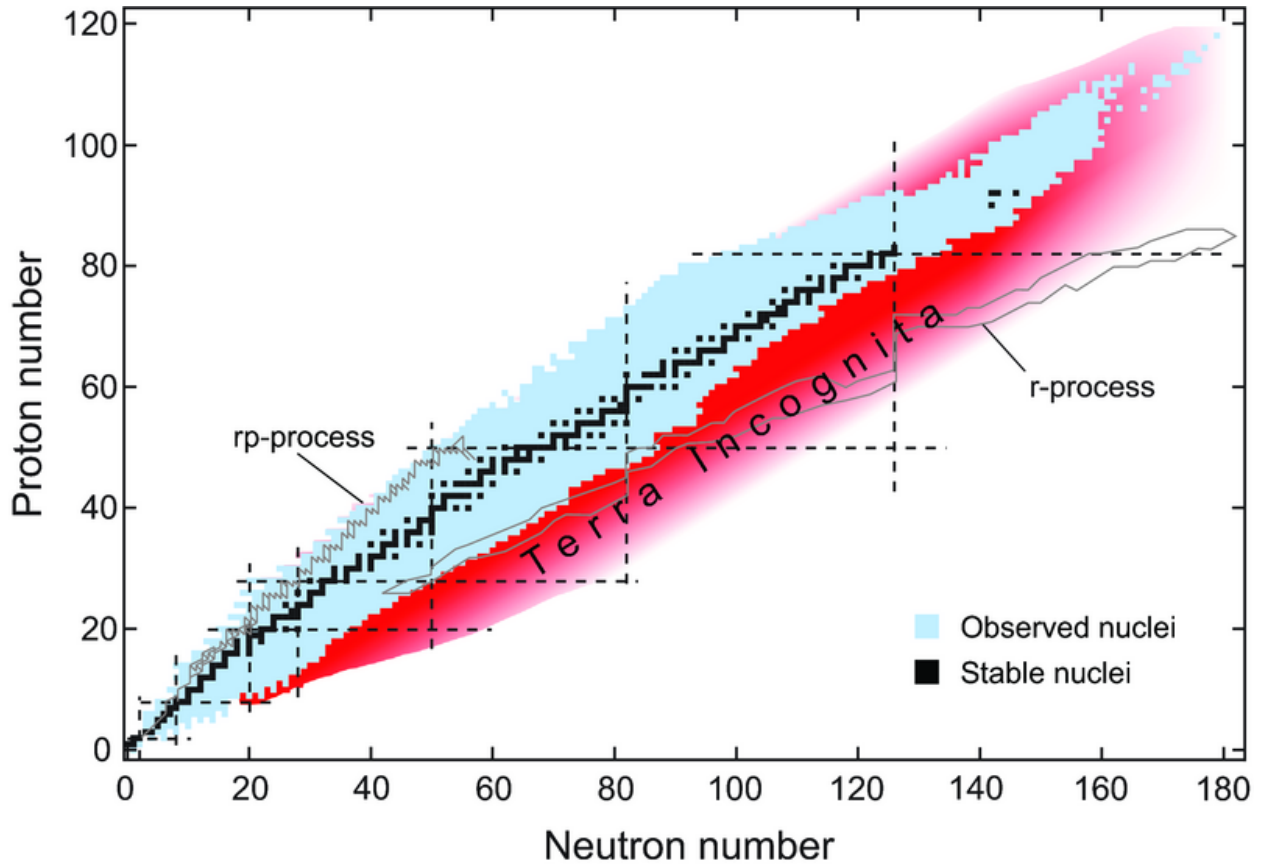


Figure 1.1: Chart of the nuclides with stable nuclei shown as black squares [8]

the present work the experimental data only provided information on the final products of the reaction, rather than the pathway. In the two-step model, the first violent collision step proceeds quickly, on the time scale of the beam nucleus traversing the target nucleus, and a second, slower statistical deexcitation step follows [13,14]. Mass loss occurs in both steps of the reaction, though there is no experimental information about the mass loss in the fast step of the reaction relative to that in the slow step. The goal of the present work was to determine the mass loss in the fast step and the associated excitation energy.

Several models exist to describe the fragmentation process. The abrasion/ablation model is a geometric description where a portion of the projectile is said to be abraded in the interaction with the target, resulting in an excited prefragment; this prefragment then deexcites by the emission of particles and gamma rays to form the final fragment. The excitation energy is the energy imparted to the prefragment in the abrasion step of the reaction and

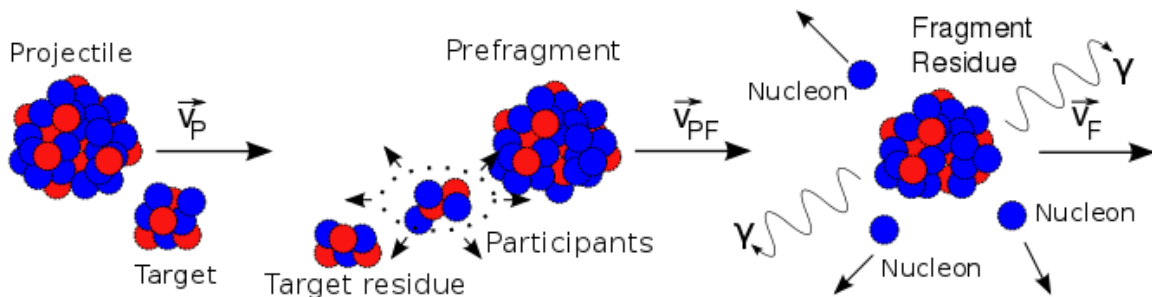


Figure 1.2: Schematic representation of a projectile fragmentation reaction in the two-step abrasion/ablation model

is subsequently lost in the ablation step. The internuclear cascade models offer a more microscopic view of the reaction, with the excitation energy and mass-loss being generated from nucleon-nucleon collisions between the projectile and target. The abrasion/ablation and internuclear cascade models produce the same general trend for the intermediate products, with excitation energy increasing as a function of mass loss, but with widely varying magnitudes.

The studies carried out in this work determined the mass of the precursor fragment and excitation energy by measuring charged fragments in coincidence with neutrons in a projectile fragmentation reaction. The experiment was conducted at the National Superconducting Cyclotron Laboratory using the Modular Neutron Array [15] in conjunction with the Sweeper magnet [16]. A ^{32}Mg beam was made incident on a ^9Be target to produce a fragment residue and neutrons. The use of a neutron-rich projectile enhanced neutron emission from the prefragment and suppressed charged-particle emission. The number of neutron hits recorded for each detected sodium, neon, and fluorine isotope was compared by a χ^2_ν analysis to the output from a statistical evaporation model [17] to determine the best precursor mass and

excitation energy.

Chapter 2

FRAGMENTATION REACTIONS

The net or final reaction products from projectile fragmentation reactions provide a reliable foundation for beam facilities such as NSCL. However, the detailed mechanism of this reaction is not well understood, particularly for neutron-rich nuclei. The reaction is often described by a simple abrasion/ablation model [13, 14] or a more complex internuclear cascade model [18]. The abrasion/ablation and internuclear cascade models produce very different distributions of intermediate nuclei but similar distributions of final products [19]; the models described in detail in the following Sections 2.1 and 2.2 and the predictions for the excitation energy distributions of the intermediate or precursor fragments that will be studied in this work are summarized.

2.1 Abrasion/ablation model

The abrasion/ablation model describes the fragmentation reaction as a two-step process. The first step of the reaction is called abrasion and proceeds quickly, on a time scale similar to the time required for the nuclei to pass one another. In the abrasion step, an excited prefragment is formed by the removal of nuclear matter by the target nucleus. The prefragment is characterized by a mass (A), nuclear charge (Z), and an excitation energy (E^*). The abrasion process has been modelled on a geometrical basis, which is described below in Section 2.1.1. The subsequent ablation step occurs on a longer time scale compared to the abrasion step, and describes the overall de-excitation of the prefragment, eventually forming the final, observed product. The prefragment loses energy in the ablation step by the isotropic emission of various particles and gamma rays. The entire reaction process is illustrated schematically in Figure 1.2. [13, 14]

2.1.1 Excitation energy generation in the abrasion/ablation framework

The excited state of the prefragment from the abrasion process is usually only described by the excitation energy, as the angular momentum transfer is thought to be small [20]. The energy and multiplicity of the decay particles from the de-excitation of the prefragment are then correlated to the excitation energy. Thus, a measurement of the excitation energy would provide new insight into both steps of the reaction and was the goal of the present work. Two approaches have been developed to model the excitation energy: macroscopic and microscopic. The macroscopic approach considers the nucleus as a single, uniform object, while the microscopic approach treats individual nucleons. In general, a strict correlation between the excitation energy and mass loss is predicted by both frameworks. The predictions from the macroscopic model of the fragment excitation energy are presented next, followed by the predictions from the microscopic model

2.1.2 Macroscopic excitation model

The abrasion-ablation model proposed some time ago by Bowman et al. [14] was intended to describe the mass distributions observed in relativistic heavy ion projectile fragmentation reactions. In their model, the target and projectile nuclei are assumed to be hard spheres that move along straight-line trajectories, making clean cuts through one another during the reaction. Thus, the number of nucleons removed can be obtained from a geometrical calculation of the overlap volume between a sphere and cylinder. The number of removed nucleons, called participants, in a spherical nucleus with mass number A_1 has been approximated as [21]:

$$N_1 = A_1 F(\nu, \beta) \tag{2.1}$$

where ν specifies the relative sizes of the interacting nuclei and β the reduced impact parameter:

$$\nu = \frac{R_1}{R_1 + R_2} \quad (2.2)$$

and

$$\beta = \frac{b}{R_1 + R_2} \quad (2.3)$$

As presented by Bowman et al. [14] and later given analytically by Gosset et al. [21], in a peripheral collision where $R_T < R_P$ and the subscripts refer to the target and projectile respectively, the removal function is:

$$F(\nu, \beta) = \frac{3}{4}(1 - \nu)^{1/2} \left(\frac{1 - \beta}{\nu} \right)^2 - \frac{1}{8} \left(\frac{3(1 - \nu)^{1/2}}{\mu} - \frac{[1 - (1 - \mu^2)^{3/2}][1 - (1 - \mu)^2]^{1/2}}{\mu^3} \right) \left(\frac{1 - \beta}{\nu} \right)^2 \quad (2.4)$$

Equation 2.4 represents the case of a cylindrical channel gouged in the projectile with a radius smaller than that of the projectile. This geometric approach to determining the mass removed in the fast step of the reaction has been shown by Morrissey et al. [22] to be consistent with the distribution of target nuclei created by these reactions when a smaller projectile interacts with a larger target.

The minimum excitation energy for the remaining spectator nucleons, which form the prefragment shown in Figure 1.2, comes from the excess surface energy of the severely deformed intermediate object. The excess surface energy is the extent to which the surface area of the prefragment deviates from the minimum value for a sphere with that mass number. The excess surface area can be written as:

$$\Delta(\text{area}) = 4\pi R_1^2 \left[1 + P(\mu, \nu, \beta) - (1 - F(\nu, \beta))^{2/3} \right] \quad (2.5)$$

where $P(\mu, \nu, \beta)$ is a function that is again dependent on the relative sizes of the target and projectile and the impact parameter of the collision, and $F(\nu, \beta)$ was defined in Equation 2.4.

For the case above, where $R_T < R_P$ and a peripheral reaction:

$$P(\mu, \nu, \beta) = \frac{1}{8} \sqrt{\mu\nu} \left(\frac{1}{\mu} - 2 \right) \left(\frac{1-\beta}{\nu} \right)^2 - \frac{1}{8} \left[\frac{1}{2} \sqrt{\nu/\mu} \left(\frac{1}{\mu} - 2 \right) - \frac{[(1/\nu)(1-\mu^2)^{1/2} - 1][(2-\mu)\mu]^{1/2}}{\mu^3} \right] \left(\frac{1-\beta}{\nu} \right)^3 \quad (2.6)$$

where $\mu = (1/\nu) - 1 = \frac{R_2}{R_1}$. The excitation energy from the excess surface energy is given by the surface tension coefficient $\gamma = 0.95 \text{ MeV/fm}^2$ times the change in area in fm^2 : [21]

$$E_{\text{surf}} = 0.95 \times \Delta(\text{area}) \quad (2.7)$$

The resulting excitation energy thus depends only on the geometry of the collision and not on the incoming particle energy. Oliveira et al [23] have shown that the excitation energy from the excess surface energy is generally not adequate to describe the overall reaction process as seen in the distribution of final products. Oliveira et al. proposed the addition of a frictional spectator interaction (FSI), which adds a component to the excitation energy from the rescattering of spectator nucleons within the excited prefragment by the participants that leave the interaction zone. This formalism is based on individual nucleon-nucleon collisions and gives the average deposited energy, $\langle E_{\text{FSI}} \rangle$ as:

$$\langle E_{\text{FSI}} \rangle = \frac{1}{\pi} \int_0^\pi E_{\text{dep}}(\theta) d\theta, \quad (2.8)$$

where $E_{\text{dep}}(\theta)$ is a function that describes the amount of energy that is deposited in the nuclear material as a function of angle relative to the beam direction. Oliveira et al. determined that the total excitation energy of the prefragment could be given by

$$E^* = E_{\text{surf}}(\Delta A_{\text{abr}}) + m_{\text{FSI}} \langle E_{\text{FSI}} \rangle, \quad (2.9)$$

where the second term has to be computed for each collision geometry with m_{FSI} specifying the number of interactions and $\langle E_{\text{FSI}} \rangle$ the magnitude. Wilson et al. [24] proposed a simpler, geometric solution to this secondary contribution based on the rate of energy loss of a nucleon

passing through uniform nuclear matter, estimated at 13 MeV/fm. Wilson et al. arrived at the expression for excitation energy, E_x :

$$E_x = 13C_1 + \frac{1}{3}13C_1(C_t - 1.5) \quad (2.10)$$

where C_1 is the maximum distance travelled by any participant nucleon through the projectile and C_t is the maximum chord transverse to the projectile velocity spanning the projectile surface interface, describing the target constituents in the interaction region. Wilson et al. also described the total excitation energy as the sum of the excess surface energy and the rescattering term (E_x). The final expression of Wilson et al. for the excitation energy, E^* , is:

$$E^* = E_{\text{surf}} + E_x \quad (2.11)$$

$$= (0.95 \times \Delta(\text{area}) \times f) + 13C_1 + \frac{1}{3}13C_1(C_t - 1.5) \quad (2.12)$$

where the surface energy term has been further modified by the introduction of an additional frictional term f , which accounts for an additional excitation that is a function of the number of abraded nucleons:

$$f = 1 + 15 \frac{\Delta_{\text{abr}}}{A_P} + 25 \frac{\Delta_{\text{abr}}^2}{A_P^2}. \quad (2.13)$$

The total calculated excitation energy as a function of abrasion mass loss for the Wilson model is shown in Figure 2.2 for fragments produced from a ^{32}Mg beam.

2.1.3 Microscopic excitation model

Microscopic models for excitation energy deposited in the abraded prefragment have been based on the effect of collisions between individual nucleons. One such description by Gaimard et al. [25] assumed that the excitation energy is due to vacated single-particle levels, or “holes”, in the Fermi sea from a Woods-Saxon potential of the nucleus before the collision. Gaimard et al. asserted that the excess surface energy model for excitation energy is invalid, as the wave functions of the spectator nucleons are not disturbed by the fast

process, and thus it is unreasonable to assume that energy is imparted to them from the breaking of nucleon-nucleon bonds. Instead, their suggestion is that the orbits of the nucleons removed in the collision are preserved, thus creating single-particle holes in the energy-level scheme. In a Woods-Saxon potential, the mean energy from a hole in a randomly chosen single-particle level has been determined to be 13.3 MeV [25]. The calculated excitation energy is thus a linear function of mass loss in the abrasion process, and the E^* values from the present case can be compared to those from the macroscopic model in Figure 2.1. The microscopic values are significantly higher, but track with those from the macroscopic model of the excitation energy as a function of abraded mass loss, $A_b - A_f^*$.

The microscopic model is only valid when the prefragment is not thermalized during the abrasion process. Thermalization would imply that the orbits are rearranged. An estimate of the fraction of the excitation energy which is thermalized in the abrasion process was derived in Ref. [25]. The intrinsic equilibration time is defined as:

$$\tau_{\text{intr}}(t) = 2 \times 10^{-22} \text{MeV} \cdot s / e^*(t) \quad (2.14)$$

where $e^*(t)$ is a function describing the excitation energy per nucleon in the system as a function of time. $e^*(t)$ for a peripheral collision was assumed to grow linearly as a function of time:

$$e^*(t) = \alpha t, \quad (2.15)$$

where

$$\alpha = \frac{E^*}{A^* t_1}, \text{ and} \quad (2.16)$$

where E^* is the total excitation energy, A^* is the total mass of the prefragment, and t_1 is the time required for the abrasion process. The excitation energy per nucleon that is not thermalized during the abrasion process, e , is derived from the expression:

$$\frac{de}{dt} = \alpha - \frac{e}{\tau_{\text{intr}}} = \alpha - \alpha \frac{et}{2 \times 10^{-22} \text{MeV} \cdot s} \quad (2.17)$$

By integration, the following is obtained:

$$e(t) = \alpha \left(\int_0^t \exp[0.5\beta t'^2] dt' \right) \exp[-0.5\beta t^2] \quad (2.18)$$

Table 2.1: Input variables for calculating the fraction of energy equilibrated during the abrasion process expressed in Equation 2.18.

A^*	t_1 (s)	E^* (MeV)	$e^*(t_1)$ (MeV/u)	$e(t_1)$ (MeV/u)	f (%)
30	2.9×10^{-23}	35	1.1667	1.10305	5.5

with

$$\beta = \frac{1}{2 \times 10^{-22} \text{MeV} \cdot \text{s}} \frac{E^*}{A^* t_1} \quad (2.19)$$

Through simulation, Gaimard et al. [25] showed that less than 20% of the energy is thermalized during the abrasion process for reactions at bombarding energies of 1 GeV/u. Therefore, that the assumption made on the lack of thermalization in such systems is reasonable. Gaimard et al. showed that the fraction of the excitation energy thermalized in the reaction becomes smaller as fewer nucleons are stripped in the abrasion process. The calculation of thermalization for the system of interest, ^{32}Mg on ^9Be at 86 MeV/u, gives a fractional thermalization of 5.5%. The parameters used for this calculation are shown in Table 2.1. The precursor mass, A^* , was taken to be the smallest mass loss that would result in a neon final fragment ($A_b - A_f^* = 2$) and the excitation energy (E^*) is consistent with the excitation energy predicted by the model for an abraded mass loss of two. The fraction of thermalization of 5.5% indicates that a small amount of thermalization is a reasonable assumption.

2.2 Internuclear cascade model

A completely different approach to the projectile fragmentation process was developed using the scattering of individual nucleons in the projectile and target. The Internuclear cascade (INC) model ISABEL [26, 27] was developed as a generalization of the original VEGAS [18] Monte Carlo simulation of proton-induced collisions. In contrast to the abrasion/ablation model, which presents a geometric view of the reaction, INC model describes the reaction as a sequence of two-body interactions between individual nucleons. The target and projectile

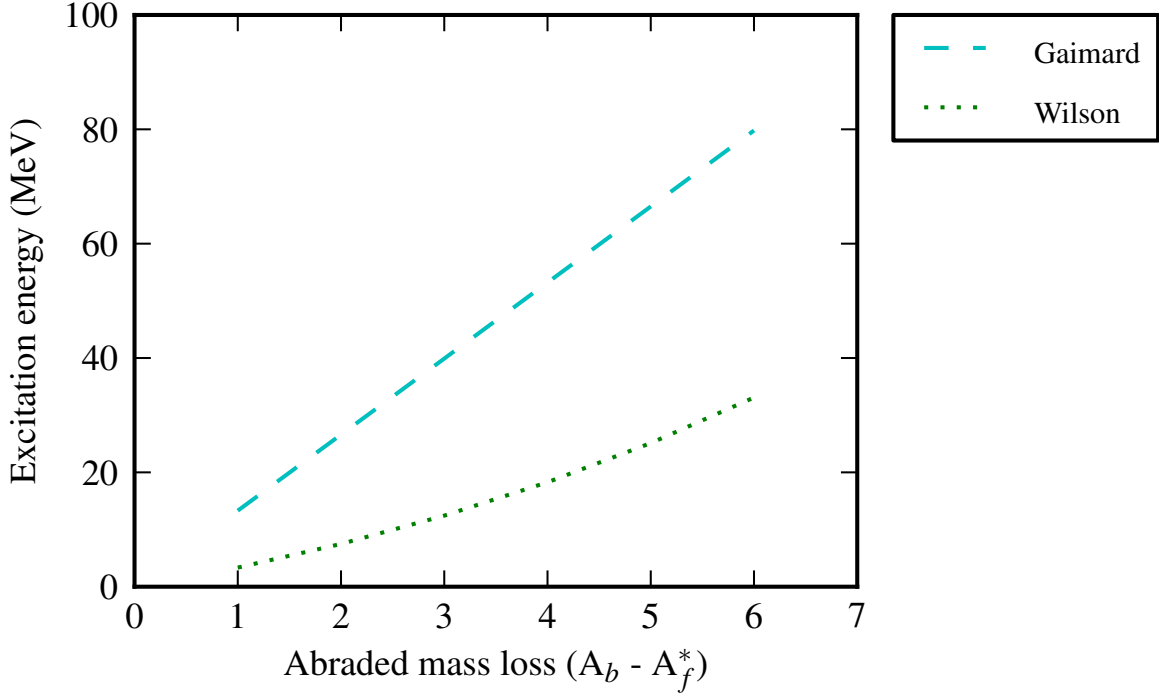


Figure 2.1: Excitation energy (E^*) versus abrasion mass loss ($\Delta A_{\text{abr}} = A_b - A_f^*$) for a macroscopic (Wilson [24]) and a microscopic (Gaimard [25]) abrasion model.

are each treated as a Fermi sea of nucleons with Fermi energy, E_F , given by:

$$E_{Fi} = \frac{\hbar^2}{2m_i} \left(3\pi^2 \rho_i \right)^{2/3}, \quad (2.20)$$

where i represents either protons or neutrons, m_i is the mass and ρ_i is either the proton or neutron density along with the usual constants. The target and projectile nucleons undergo a series of two-body interactions until the nucleons either escape the nucleus or their energy drops below a cutoff energy and they are assumed to be captured. This interaction process describes the pre-equilibrium state of the reaction, and corresponds to the abrasion step in the abrasion/ablation model. The cutoff energies for protons and neutrons are related to the average binding energy, $\langle BE \rangle$, and differ as a result of Coulomb interaction. The neutron

and proton cutoff energies are given in the INC by the expressions:

$$E_{\text{cutoff}}^{\text{neutron}} = E_F + 2 \langle BE \rangle \quad (2.21)$$

$$E_{\text{cutoff}}^{\text{proton}} = \max \begin{cases} E_F + 2 \langle BE \rangle \\ E_F + \langle BE \rangle + E_{\text{Coul}} \end{cases} \quad (2.22)$$

The nucleon interactions produce “hole” states, which contribute to the total calculated excitation energy. The total final excitation energy is the sum of the energy of the “hole” states and the kinetic energies of particles that fall below the cutoff:

$$E^* = \sum_{i=0}^{N_{\text{hole}}} E_{\text{hole}} + \sum_{i=0}^{N_{\text{particle}}} E_{\text{particle}} \quad (2.23)$$

Details of the interaction mechanism are described in Ref. [18] and are summarized below.

The probability of interaction between a beam of identical particles with momentum \vec{p}_1 and density ρ_1 and a target of identical particles with momentum \vec{p}_2 and density ρ_2 is:

$$P = \sigma_{12} \rho_1 \rho_2 v_{12}, \quad (2.24)$$

where σ_{12} is the cross section for the interaction between the projectile nucleon with momentum p_1 and the target nucleon with momentum p_2 and v_{12} is the velocity of the beam relative to the target. If the momentum distribution of the target and projectile nucleons is now considered, the probability of interaction for a given momentum \vec{p}_1 becomes:

$$P(p_1) = \rho_1 \int \sigma_{12}(\vec{p}_2) v_{12}(\vec{p}_2) \frac{\partial \rho_2}{\partial \vec{p}_2} d\vec{p}_2 \quad (2.25)$$

The probability of interaction of the particle per unit path length is thus:

$$Q = \frac{P(p_1)}{\rho_1 v_1} = \frac{1}{v_1} \int \sigma_{12} v_{12} \frac{\partial \rho_2}{\partial \vec{p}_2} d\vec{p}_2 = \lambda_1^{-1}, \quad (2.26)$$

where λ_1 is the mean free path. The probability of a bombarding particle to interact between a and $a + da$ follows a Beer’s law attenuation:

$$dN(a) = e^{-Qa} Q da. \quad (2.27)$$

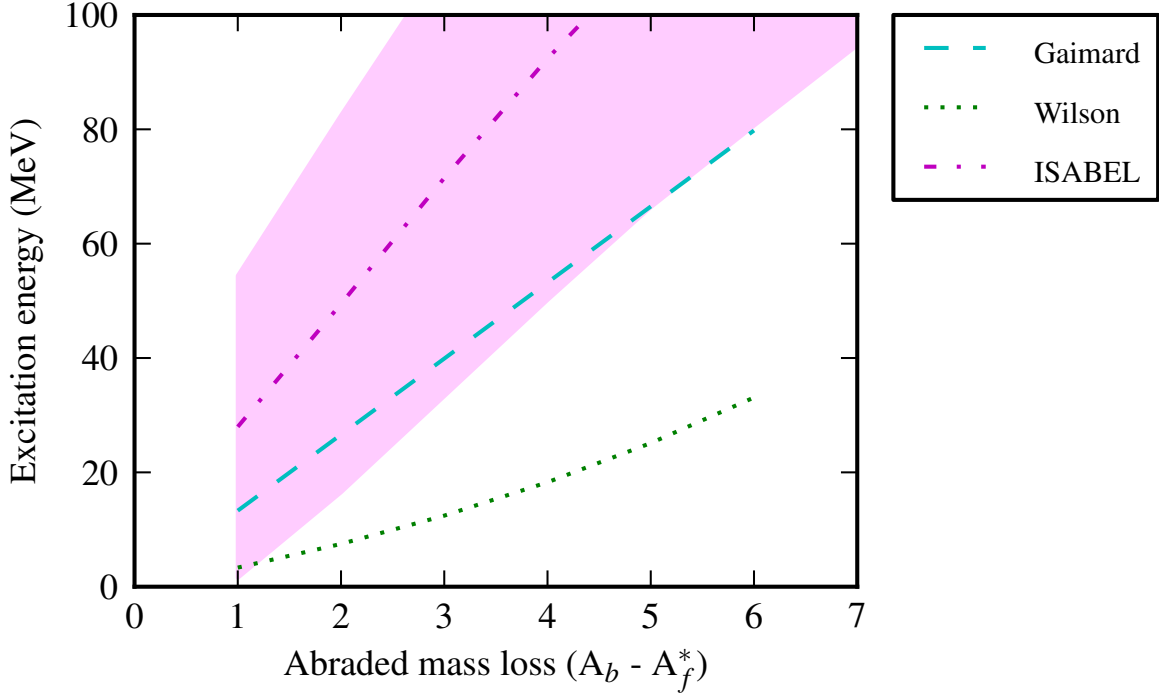


Figure 2.2: Excitation energy (E^*) versus abrasion mass loss ($\Delta A_{\text{abr}} = A_i - A^*$) for a macroscopic model (Wilson [24]), a microscopic model (Gaimard [25]) and an INC calculation (ISABEL [27], [26]) for the reaction of ^{32}Mg with Be. ISABEL line represents the average E^* found for fragments with $Z=11$. The bounds of the ISABEL region are given by the RMS of the excitation energy distribution for each $A_b - A_f^*$, see the text.

Therefore, the probability of interaction over the whole volume, a is

$$N(a) = 1 - \exp(-Qa) = 1 - \prod_{i=1}^n \exp\left(-\frac{1}{n} \rho \sigma'_i\right) \quad (2.28)$$

and the probability of interaction in the volume $\delta a = \frac{a}{n}$ is:

$$N(\delta a) = 1 - \exp(-\rho \sigma'_i \delta a). \quad (2.29)$$

The physical location of the collision and target nucleon with which the given projectile nucleon interacts are determined by comparison of the probability, $N(\delta a)$, to a random number, and the cross section σ'_i is determined from an interpolation of cross section data for nucleon-nucleon scattering.

The results from a calculation of the INC model ISABEL taking parameters from the present experimental conditions are shown in Figure 2.2. The average excitation energy for

each $A_b - A_f^*$ intermediate product is shown for the Z=11 prefragments from a ^{32}Mg beam reacting with a ^9Be target at 86 MeV/u. A key feature of INC models is that a wide range of excitation energies is generated for a given $A_b - A_f^*$. The RMS value of the excitation energy distribution for each precursor fragment mass is shown by the band in the figure. Notice that the macroscopic and microscopic abrasion/ablation and INC models all predict a general increase in E^* with $A_b - A_f^*$ but with significantly different values.

2.3 De-excitation of prefragments

The probability of an excited prefragment to decay into a final fragment is dependent on the overlap between the initial and final states. This overlap is quantified in the transition probability, given by Fermi's goldern rule [28]:

$$\lambda = \frac{2\pi}{\hbar} |V_{fi}|^2 \rho_f \quad (2.30)$$

where λ is the transition probability, ρ_f is the density of states, and $|V_{fi}|$ depends on the wavefunctions of the initial and final states (ψ_i and ψ_f respectively):

$$|V_{fi}|^2 = \left| \left(\int \psi_f^* V_P \psi_i d\tau \right) \right|^2 \quad (2.31)$$

Statistical evaporation models provide an analytic solution to Equation 2.30. One such model is the projection angular-momentum, coupled evaporation model that has been implemented in the computational code PACE [17]. PACE can be used to calculate the transition probabilities and level densities that provide a framework to calculate the emission of particles and thus the probability of decay of the excited prefragment into a given final fragment. PACE determines these transition probabilities from a full optical model calculation using the spin-dependent level density, in which the rotational energy is subtracted from the excitation energy:

$$\rho_f(E, J) = \rho_0(U)(2J + 1)\exp(2[a(U - E_{\text{rot}}(J))]^{1/2}) \quad (2.32)$$

Table 2.2: Sample input file for PACE calculation

Parameter	Value	Description
NCASC	40000	Number of cascades in Monte Carlo calculation
INPUT	2	Type of input
FYRST	0	Determines which yrast line will be used to give E_{rot}
BARFAC	0	Fission barrier
ARATIO	1	Ratio of Fermi gas level density parameter to ground state value
FACLA	10	Level density
IDIST	1	Format of output file
MDIR	0	Spin projection state of the compound nucleus
ITRAC	0	Format of output file
NOSHL	0	Mass values (NOSHL=0 uses AME2003)

where $U = E - P$ and P is the pairing energy; ρ_0 is determined by the Gilbert and Cameron formalism [29] and E_{rot} is determined by calculation [17]. A modified version of PACE [?] was used in the present work to simulate the decay of excited prefragments, in which the rotational energy, E_{rot} , and level density ρ_0 [29] are given in the input file [30]. The deexcitation process is accomplished with a Monte Carlo procedure, with the number of deexcitation cascades given in the input file. A sample input file can be seen in Table 2.2.

The evaporated neutrons are emitted isotropically in the center-of-mass frame when angular momentum is not important, but are forward focused in the lab frame due to the high velocity of the initial secondary beam, as illustrated in Figure 2.3. Therefore, these neutrons can be detected efficiently in a detector system that is placed near or around zero degrees in the lab frame.

Up to the present, only the overall effects of the variation of excitation energy with mass-loss on the final fragment mass and charge distributions have been studied. That is, the mass and charge distributions have been interpreted in terms of assumed correlations of the excitation energy with abrasion mass loss [19], [31] or the momentum distributions of the final products have been interpreted in terms of a fast abrasion and a slow evaporation process [22], [32]. In the present work, the de-excitation neutrons were measured in coincidence with

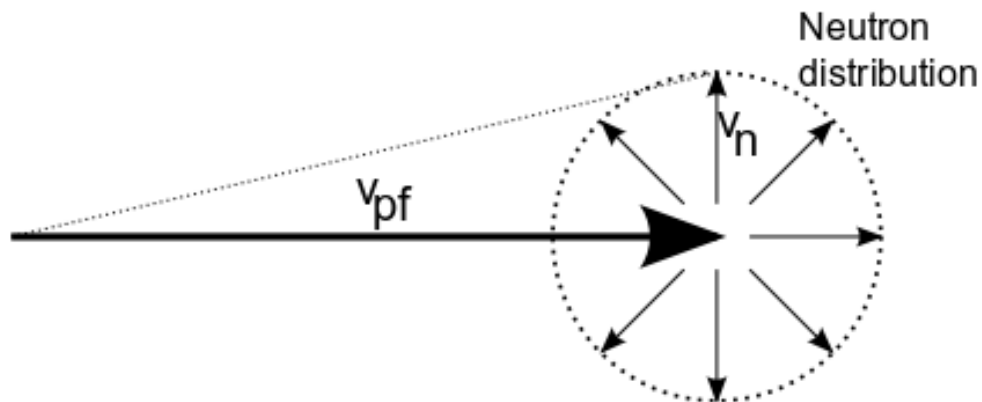


Figure 2.3: Schematic view of the evaporation of neutrons from the excited prefragment as an isotropic process in the rest, when angular momentum is not important. However, due to the high forward momentum of the prefragment in the lab frame, the evaporated neutrons become highly forward focused.

the final fragments. These new measurements provided a new insight into the reaction mechanisms and were able to differentiate among the predictions of the reaction models.

Chapter 3

EXPERIMENTAL DETAILS

3.1 Beam characteristics

3.1.1 Primary beam

A sample of ^{48}Ca was ionized by an electron cyclotron resonance (ECR) ion source and injected to the K500 cyclotron at NSCL. The the K500 and K1200 were used to accelerate the beam to 12.32 MeV/nucleon and 140 MeV/nucleon, respectively. The final beam was produced in a fully stripped state, *i.e.* a charge of 20^+ . This beam impinged on a 1316 mg/cm² thick natural beryllium target to produce the ^{32}Mg secondary beam necessary for the present work. The ^{32}Mg secondary beam was then separated out from the other reaction products by the A1900 fragment separator [1].

3.1.2 Secondary beam

The A1900 fragment separator can produce a secondary beam by the combination of magnetic selection and energy loss in a solid degrader that selects individual isotopes. The separation is based on mass-to-charge ratio and is accomplished by selecting products according to a bend radius in a magnetic field. The force on a particle with charge q moving through a magnetic field with strength \vec{B} and velocity \vec{v} is

$$\vec{F} = \frac{d\vec{p}}{dt} = q\vec{v} \times \vec{B}. \quad (3.1)$$

Integrating with respect to time on both sides of Eq. 3.1 and taking $p(t_o) = 0$ and $v(t_o) = 0$ with a magnetic field which is constant over time,

$$p = mv = qB\rho \quad (3.2)$$

or

$$B\rho = \frac{mv}{q} \quad (3.3)$$

Variations in the mass-to-charge ratio for different beams are directly proportional to changes in the magnetic rigidity, causing the paths of the beams through the series of dipole magnets in the A1900 to be different.

The magnetic rigidities of the four superconducting dipole magnets, which constitute the segments of the spectrometer, were set to the calculated rigidity of the secondary beam. An aluminum achromatic wedge with thickness 600 mg/cm^2 , placed at the intermediate focal plane at the midpoint of the separator, was used to select the ^{32}Mg secondary beam. This wedge provided a unique energy loss for the isotope of interest that allowed the third and fourth dipoles to separate the desired ^{32}Mg secondary beam from the other products. Finally, slits at the intermediate image of the A1900 were used to limit the momentum acceptance to 0.5%. After exiting the A1900 fragment separator, the energy of the ^{32}Mg secondary beam was 86 MeV/u, with a beam purity of 95% and a ^{32}Mg secondary beam rate of 46 pps/pnA. The largest contaminant was ^{34}Al (see section 4.3.1).

3.2 Experimental Configuration

A schematic view of the experimental setup used to measure the excitation energy of neon prefragments is shown in Figure 3.1 and is described in more detail in the following sections. The secondary ^{32}Mg beam was focused onto the Be reaction target, with a beam spot size of $\sim 2 \text{ cm}$, by a triplet of quadrupole magnets after the beam entered the N2 vault. A thin 0.254 mm plastic scintillator was positioned just upstream of the target, to provide a start time for the neutron and particle time-of-flight (ToF). The Be reaction target was located at the object position of the Sweeper magnet [16], a 3.8 T large-gap dipole magnet.

Fragments produced following the interaction of the ^{32}Mg with the production target were bent by the Sweeper magnet, and their positions and trajectories were determined by

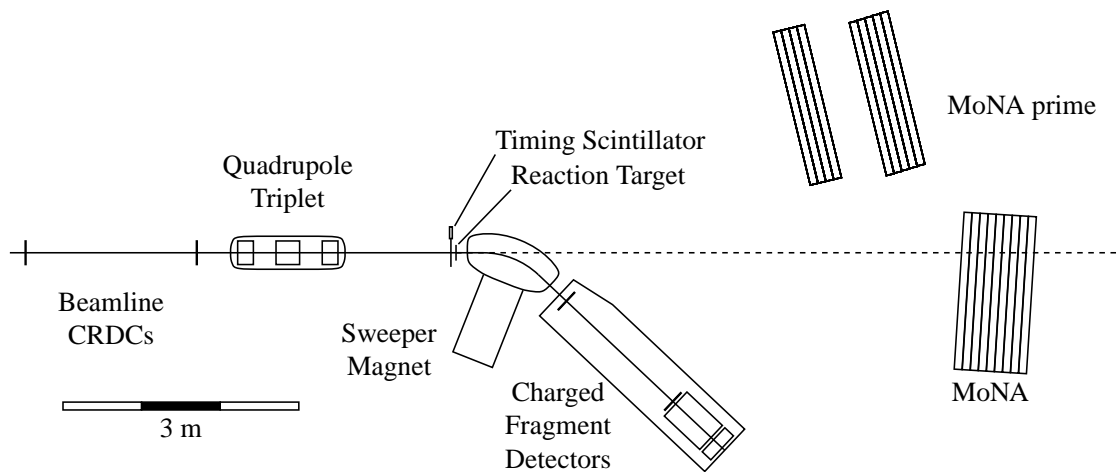


Figure 3.1: Schematic view of the Sweeper-MoNA experimental setup in the N2 vault at NSCL.

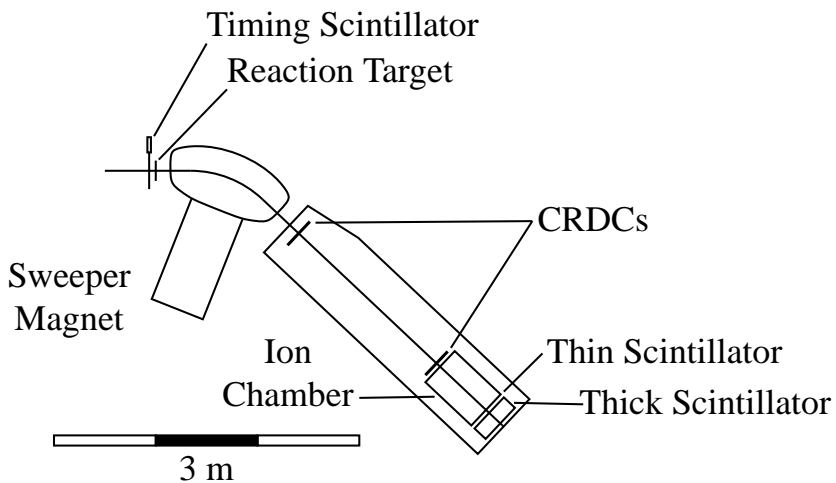


Figure 3.2: Schematic view of the charged particle detectors near the target and at the focal plane of the Sweeper magnet

two cathode readout drift chambers (CRDCs). A multi-segmented ion chamber downstream of the CRDCs was used to measure the energy loss of the charged fragments. A thin 0.5 cm plastic scintillator, placed downstream of the ion chamber, provided the master trigger for the experiment as well as a measurement of the fragment energy loss [33]. Finally, a thick, 15 cm plastic scintillator stopped the charged fragments, and was used to measure the residual energy of the charged fragments. A schematic view of these detectors is shown in Figure 3.2, and more details on the individual detectors are given below.

Neutrons produced in the reaction at the Be reaction target were forward focused due to the high beam velocity of the emitting fragments ($\sim 0.3c$). These neutrons were detected by the Modular Neutron Array (MoNA) [15]. MoNA was reconfigured from its normal arrangement of a single array centered about 0° to two stacks to maximize the horizontal angular coverage. The time of flight from the target to MoNA was used to determine total energy of the neutrons, while the segmentation of the detector was used to provide the position and angle of the detected neutrons.

3.2.1 Beam line detectors

3.2.1.1 A1900 focal plane scintillator

A 1.008 mm thick plastic scintillator made of Bicron BC-404 material was positioned at the A1900 focal plane and was the first of a pair of detectors used to measure the time-of-flight of the secondary beam. When charged particles pass through a scintillator material, some of the molecules in the material are excited. The hydrocarbons in the plastic have carbon-carbon double bonds with a conjugated π -electron structure. The interaction of charged particles with the material excites some of the electrons in these π energy levels. Light is emitted when the molecules de-excite, either promptly through fluorescence, or following inter-system crossing through phosphorescence, which has a significantly longer lifetime. The photons that are emitted during the de-excitation process are collected at the photocathode

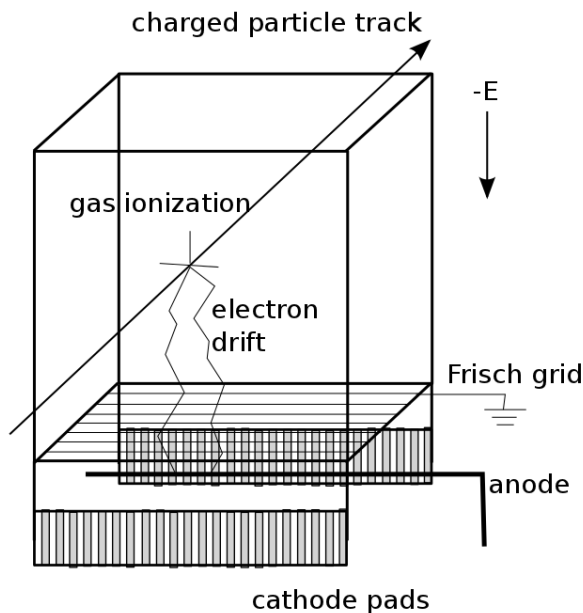


Figure 3.3: Schematic view of the operation of a CRDC from Ref. [33].

of a photomultiplier tube (PMT), where the photon signal is converted to an electrical signal, via the photoelectric effect, and amplified before finally being processed and recorded [34].

3.2.1.2 Tracking Cathode Readout Drift Chambers

Each CRDC detector was filled with a gas mixture of 80% CF_4 and 20% isobutane (C_4H_{10}) held at a total pressure of 50 Torr. Charged particles entering the CRDCs ionized the gas molecules as they passed through, creating ion pairs. A schematic of a CRDC is shown in Fig 3.3 [33]. The electrons were subjected to a vertical drift voltage of -250V , causing them to drift toward and then through the Frisch grid, and then were avalanched on the anode wire, which was held at $+1100\text{V}$. Charge collection on the anode wire induced a signal on 64 aluminum pads placed perpendicular to the wire, with a 2.54 mm pitch. The position of the charged fragment in this, the dispersive, direction was determined by the distribution of induced charge on the aluminum pads. The calibration slope for position in the dispersive direction was determined by the fixed pitch of the pads, while the offset of the absolute

position was determined by a mask calibration. The mask was a tungsten plate with holes drilled at specific locations, allowing the beam to illuminate the detector at known physical locations. The results from sample mask calibration runs are shown in Figure 4.2. The position in the non-dispersive, vertical, direction was determined by drift time from the interaction point to the anode wire. This drift time was also calibrated as part of the same mask calibration procedure. The centers of the CRDCs were positioned along the beam axis 1.723 m and 3.546 m from the target.

3.2.2 Target chamber

The target chamber in the N2 vault contained a 235 mg/cm² thick beryllium reaction target and a 0.254 mm thick plastic scintillator located 0.065 m upstream of the target. The plastic scintillator was operated in the same manner as that described in Section 3.2.1.1. The plastic scintillator provided a reference signal for the time of flight of the beam, charged particles, and neutrons. The detector was operated in the fringe field of the Sweeper magnet, so its performance was dependent on the Sweeper magnetic field.

3.2.3 Sweeper magnet

The Florida State University-Michigan State University Sweeper magnet [16] used in the present work is a dipole magnet with a maximum field of 3.8 T and a bending angle of 43°. The vertical gap of the magnet is large enough to allow forward-focused neutrons to pass through relatively unimpeded. To maintain vacuum in the magnet gap, the neutrons have to pass through a 6.4 mm thick steel plate at zero degrees referred to as the neutron window. The opening angle of the magnet at the neutron window is $\pm 12.6^\circ$ in the horizontal direction and $\pm 2.9^\circ$ in the vertical direction, with respect to the target.

To detect the widest range of isotopes of neon and neighboring elements, three different magnetic rigidity settings of the Sweeper magnet were used: 3.75 Tm (345 A), 3.15 Tm (270 A) and 2.97 Tm (250 A). The ranges of fragments that should, based on calculated rigidi-

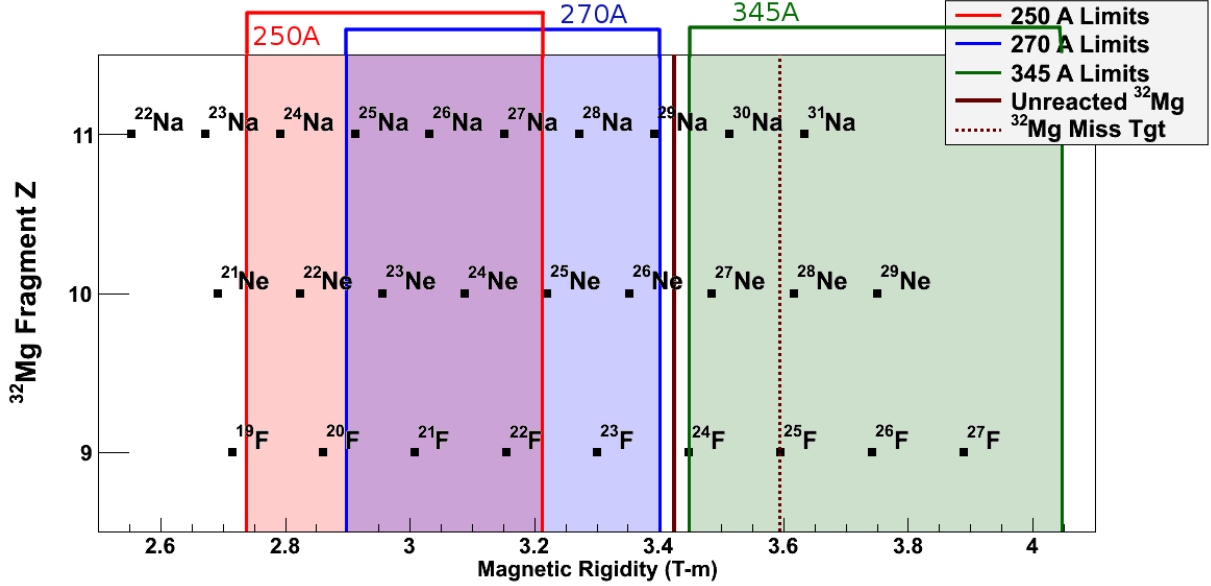


Figure 3.4: Calculated central values of the rigidities of the fragments in the focal plane of the Sweeper magnet for each of the three $B\rho$ settings used in the experiment. The settings are distinguished by the magnet current in amperes.

ties, have reached the focal plane for these settings are shown schematically in Figure 3.4. The Sweeper magnet rigidity settings were selected to give the widest range of fragments that did not allow the ^{32}Mg beam to strike any of the focal plane detectors.

3.2.4 Focal plane detectors

There were five detectors located in the focal plane box along the charged particle flight path after the Sweeper magnet. These detectors were used to fully characterize the charged particles that resulted from the interaction of the ^{32}Mg beam in the reaction target. Following the Sweeper magnet, two CRDCs were used to determine the position and angle of charged particles. The operation of these CRDCs was the same as that of the tracking CRDCs described in Section 3.2.1.2, but the detector specifications were slightly different. The focal plane CRDCs had dimension $30 \times 30 \text{ cm}^2$ and had 128 cathode readout pads with a 2.54 mm pitch. The gas pressure in each detector was maintained at 50 Torr, with the same 80% CF_4 and 20% isobutane mixture, and the anode and drift voltages were set at +950 and

-800 V, respectively. The detectors were positioned 1.82 m apart.

Downstream of the CRDCs was an ionization chamber, used to measure the energy loss needed for element identification of the reaction products. The ion chamber was filled with P-10 gas, 90% argon and 10% methane (CH_4), at 300 Torr. As with the CRDCs, charged particles that passed through the ion chamber ionized the gas, releasing electrons, which travelled through the detector in response to a -800V drift voltage. The charge was collected after passing through a Frisch grid on 16 charge collection pads each held at +1100 V. The induced signal on the pads was integrated to give a signal proportional to the energy lost in the detector.

The furthest downstream detectors were two BC-404 plastic scintillator detectors. The mode of operation for these plastic scintillators was the same as described in Section 3.2.1.1. These scintillators each had an area of $40 \times 40 \text{ cm}^2$. The large active area necessitated coupling each detector to four PMTs, with a PMT positioned at each corner of the detector along the top and bottom edges. The upstream scintillator was 0.5 cm thick and was primarily used to generate a timing signal. The downstream scintillator was 15 cm thick, sufficient to stop the ions. The charge collected in this second scintillator gave a signal related to the range of the charged fragment in the material, which is a function of the energy and nuclear charge (Z) of the fragment, and was used to identify elements generated in the reaction.

3.2.5 Modular Neutron Array

The Modular Neutron Array (MoNA) [15] consists of a gross (144) of $2 \text{ m} \times 10 \text{ cm} \times 10 \text{ cm}$ BC-408 plastic scintillator bars with a light guide coupled to a PMT on each end of each bar. For this experiment, the bars were arranged for the first time in a two-stack configuration, with one stack, henceforth referred to as “MoNA”, positioned on the beam axis, and the other, referred to as “MoNA'”, to the side of the beam axis, as illustrated in Figure 3.1. MoNA and MoNA' each contained nine layers of bars stacked eight bars high. The supporting tables were elevated such that the assembled bars were centered on the beam axis (four below and

four above). The front face of MoNA' was positioned 4.3 m downstream of the target, and MoNA 6.29 m downstream of the target. This arrangement of MoNA and MoNA' allowed for 52° of horizontal angular coverage, from +39° to -13°.

The neutrons generally interacted with the protons (hydrogen nuclei) within the plastic. When a neutron directly struck a proton, the proton recoiled out of the molecular structure, generating excitations and finally scintillation light in the manner described in Section 3.2.1.1. These photons traversed the length of the scintillator, in both directions, and were transmitted by the light guides into the PMTs at the bar ends. The time difference between the signals observed at the end of each bar was used to determine the horizontal (x) position of the neutron event by the relation:

$$\Delta t = \frac{1}{2} (t_l - t_r) \quad (3.4)$$

The vertical (y) and longitudinal (z, the beam direction) positions of a neutron interaction were determined by the discretization of the array; namely, which bar registered the hit. As each bar in the array has dimension 2 m x 10 cm x 10 cm, the y and z position measurements had an uncertainty of ±5 cm.

3.2.6 Electronics and Data acquisition

The electronics and data acquisition (DAQ) for both the neutron array (MoNA and MoNA') and the Sweeper setup have been described in detail in Refs. [35], [36] and [37], so only a brief summary is provided here. For each event, charge and time signals were recorded for both the charged particle and neutron detectors. Each MoNA/MoNA' PMT has two signal outputs, from the anode and the dynode. The anode signals were used for the timing signals. The signals were passed through constant fraction discriminators (CFDs) to convert the signals to logic pulses and finally to time-to-digital converters (TDCs) to be recorded. The dynode signals were inverted and then processed by charge-to-digital converters (QDCs) and read out.

Table 3.1: Logic signals sent between the Sweeper and MoNA/MoNA' subsystems. Valid time signals must surpass the CFD threshold

Logic signal	Description
Sweeper trigger	Valid time signal in the thin scintillator upper left PMT
MoNA trigger	Valid time signal in any MoNA PMT
MoNA valid	Valid time signal from both PMTs on at least a single bar
System trigger	Valid time signal in the thin scintillator upper left PMT
Busy	The system is working to process event data

A description of the logic signals used in this experiment in the MoNA/MoNA'-Sweeper setup is outlined in Table 3.1. This experiment was operated in “singles” mode, meaning the system trigger only required a valid signal from the thin scintillator in the Sweeper focal plane. Thus, events were recorded regardless of the presence of a neutron signal, allowing neutron multiplicity zero events to be recorded. The timing signals from the MoNA/MoNA'/Sweeper setup are illustrated schematically in Figure 3.5. As just described, the master trigger for the experiment was the thin plastic scintillator at the Sweeper focal plane. The logic time signal was generated by a CFD that provided a digital NIM logic pulse before being sent to the Level 2 logic module, an FPGA (field-programmable gate array), which provided the trigger logic for the whole system. This trigger signal opened a 250 ns coincidence window for events from MoNA/MoNA'. The presence of a valid neutron event was determined by the Level 1 logic modules by requiring signals from both PMTs on at least one MoNA or MoNA' bar. The general logic conditions are given in Table 3.1. The experiment was run over a period of 5 days with a total of 8×10^5 fragments observed and 4×10^5 neutron coincidences. The analysis of this data is discussed in the following chapter.

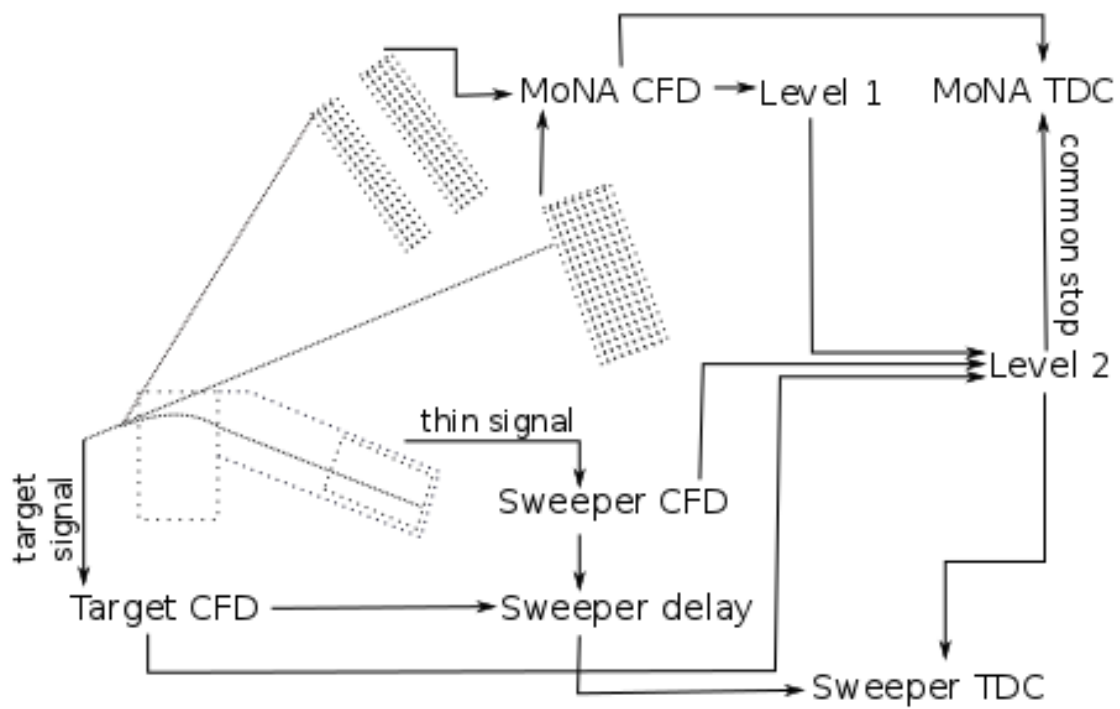


Figure 3.5: A schematic diagram of the combinations of the timing signals for the MoNA/MoNA' and Sweeper electronics used to form the Level 1 and Level 2 triggers.

Chapter 4

ANALYSIS

4.1 Overview

The goal of the present analysis was to extract the excitation energy of precursor fragments formed in the fragmentation of ^{32}Mg ions in a ^9Be target. Coincidences between a range of sodium, neon, and fluorine projectile fragments detected in a tracking detector system and neutrons detected in a large position-sensitive array were analyzed to extract the excitation energy distributions. The experimental devices described in the previous chapter were calibrated following the procedure outlined in Section 4.2. The multiplicity information from the neutron detectors was then compared to the output of neutron evaporation simulations described in Section 5.2 and a χ^2_ν analysis was performed to determine the best excitation energy and prefragment for each detected fragment.

4.2 Calibrations

4.2.1 Neutron detectors: MoNA/MoNA'

The neutron detectors were calibrated prior to the experiment using cosmic ray muons. These muons are a result of a cosmic ray interaction in the upper atmosphere, creating a shower of pions. The pions then decay into fast-moving muons, generally at $v=0.98c$, and arrive at the earth's surface with a flux of roughly $1/\text{m}^2/\text{s}$ [38]. The decay of a high-energy cosmic ray is illustrated schematically in Figure 4.1. These muons interact with the MoNA/MoNA' bars, depositing the electron-equivalent of 22 MeV each. As the muons travel at a constant velocity and deposit a consistent, known amount of energy, cosmic muons are ideal for offline calibration of these scintillator bars.

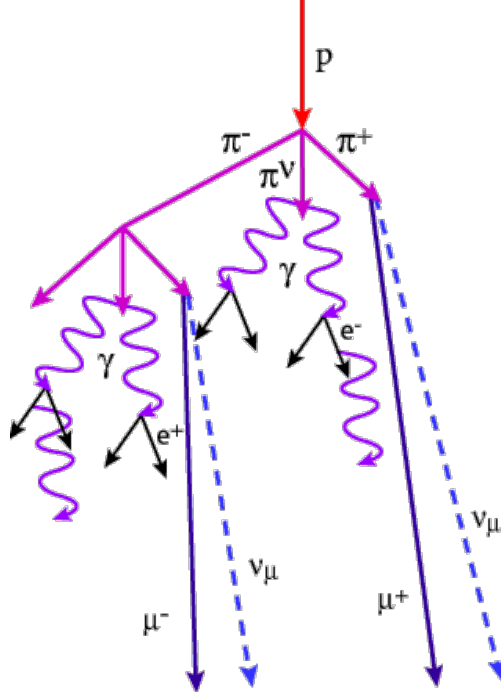


Figure 4.1: Schematic representation of an air shower resulting from the interaction of a high-energy cosmic ray, in this case a proton, with the atmosphere [39]. The scattering and decay angles are greatly exaggerated.

Small variations in PMT voltage and photocathode performance in the 144 MoNA/MoNA' bars result in variations in the observed light output from cosmic ray events. A gain-matching procedure was established to ensure that the energy measurements by the PMTs on each bar are consistent. Prior to the experiment, cosmic ray data were collected for all PMTs, and the observed charge signal was used to calibrate the relative energy output of each PMT. The charge distribution signal for each bar was collected from the inverted dynode signal from the PMT and input into a QDC, from which the digital signal was registered and found to be proportional to the energy deposited in each bar. The individual energy spectra were found to contain a single peak from the muon interactions and a first order polynomial fit was established such that the channel number of the centroid was set to the known energy deposited by cosmic muons and the smallest recorded channel number was set to zero energy.

The anode signals from MoNA/MoNA' were processed by a CFD followed by a TDC,

which digitized the time difference between the signal from each PMT and the master trigger signal. The TDCs were calibrated with a time pulser, which provided a single set of reference signals to all TDCs simultaneously.

The absolute time delay of the neutron signals was determined on-line using the so-called gamma flash from the target. Gamma rays from reactions in the target also interact with MoNA/MoNA', although with a much lower efficiency, and travel a known distance to MoNA/MoNA' from the target. As the gamma rays travel with a known velocity, $v = 1.0c$, this time difference provides an absolute time calibration. The time-of-flight to the central bar of the first layer in MoNA and MoNA' was calibrated using the gamma flash, while the relative positions of the other bars were determined using cosmic muons. Muons which travelled through the array at various angles were used to tie the time distributions of the layers together.

Finally, the horizontal position of interactions in MoNA/MoNA' was calibrated, again using cosmic muons. The horizontal position of the event was determined from the time difference between signals from the PMTs that were mounted on each end of a bar:

$$\Delta t = \frac{1}{2} (t_l - t_r) \quad (4.1)$$

The times were measured in ns, and thus a conversion to position from time difference was needed. The effective ends of the bars were defined as the points at which the time spectra reached $\frac{1}{3}$ of its maximum height in the cosmic muon data. The slopes and offsets of the position calibration were then found using the expressions

$$m = \frac{200}{t_{l(\text{end})} - t_{r(\text{end})}}, \quad (4.2)$$

and

$$b = -m \frac{t_{l(\text{end})} + t_{r(\text{end})}}{2}, \quad (4.3)$$

where m is the slope, b is the offset, and $t_{l(\text{end})}$ and $t_{r(\text{end})}$ are times at which the time spectra reaches $\frac{1}{3}$ of its maximum height.

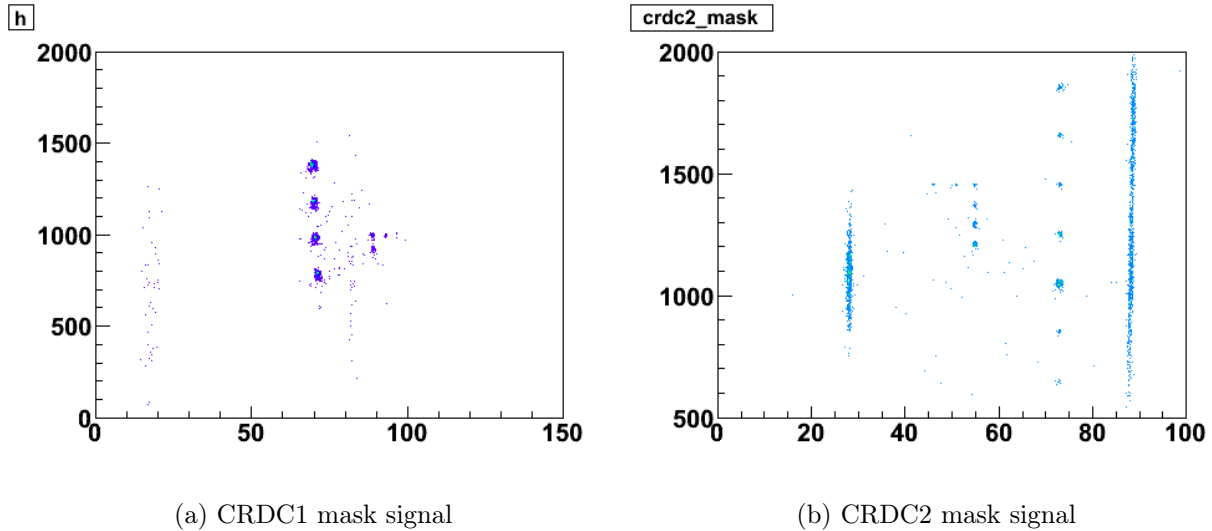


Figure 4.2: Typical mask images obtained for calibration are shown for the two cathode readout drift chambers (CRDCs) located after the Sweeper magnet. The holes in the mask were used to determine the slopes and offsets for the position calibration. A ^{28}Mg beam was used for these mask calibrations.

4.2.2 Charged particle detectors

4.2.2.1 Cathode readout drift chambers

The positions of charged particles that passed through the CRDCs were determined by fitting a Gaussian function to the distribution observed on the readout pads for the horizontal position and using the drift-time for the vertical position. The slope for the horizontal calibration was determined by the physical pad pitch (2.54 mm). The offset was determined by a mask calibration with holes in known positions to define relative positions. The vertical calibration parameters were determined from a linear fit of the observed signals to the known hole positions. The calibration spectra from the CRDCs in the focal plane can be seen in Figure 4.2.

4.2.2.2 Scintillators

The PMTs attached to the plastic scintillators used for charged-particle detection needed to be gain matched. This calibration was completed after the experiment and then applied to

the data prior to analysis. A reference signal was obtained by setting the Sweeper magnet such that the unreacted ^{32}Mg beam struck the middle of the focal plane detectors. The energy signal of the unreacted beam in the center of the scintillators was found to be roughly constant with respect to the small variations in position, and thus the response from the four different PMTs for each scintillator was mapped to a constant energy.

The response of the thin plastic scintillator was also corrected for any position dependence by sweeping the unreacted ^{32}Mg across the focal plane. The trajectories of the incoming particles were determined from the CRDCs in the focal plane. A second order polynomial function was necessary to correct the observed variation of the signal of the scintillator, with parameters given in Table 4.1.

Finally, the scintillator signals were aligned in time also using the unreacted ^{32}Mg beam. The known physical detector positions and kinetic energy of the beam were used to calculate the timing offsets for the thin and thick scintillators. From the $B\rho$ of the final segment of the A1900, the kinetic energy of the ^{32}Mg beam was calculated to be 85 MeV/u at the thin timing scintillator preceding the target. Based on LISE++ [6] calculations, the beam lost 253 MeV going through the target. The time offset for the PMT on the upper left corner of the thin scintillator was set to the time-of-flight of a ^{32}Mg beam particle from the target timing scintillator to the thin scintillator of 36.02 ns. Offsets for the other three PMTs were set to align the other signals in time.

4.2.2.3 Ion chamber

The signals from the 16 pads of the ion chamber were also gain matched using the unreacted ^{32}Mg beam. A slope for each pad was determined by aligning the means of the collected charge signals from unreacted ^{32}Mg beam to a consistent but arbitrary value. The position-sensitive CRDCs upstream from the ion chamber were then used to correct for the signal, based on the trajectories of the incoming particles. The parameters for this correction are also given in Table 4.1.

Table 4.1: Correction parameters for the thin scintillator and ion chamber positions

Corrected signal	Position	Zeroeth order	First order	Second order
Thin scint energy	Thin x-pos	660.1	0.057	-0.0037
Ion chamber summed signal	Thin x-pos	457.3	-0.592	N/a

4.3 Charged fragment identification

The detectors at the end of the flight path downstream of the Sweeper magnet, shown schematically in Figure 3.2, were used together to identify the mass and charge of each fragment. These charged fragments were then correlated on an event-by-event basis with corresponding neutron events that were detected in MoNA/MoNA'. The following sections describe the process used to identify the charged fragments.

4.3.1 ^{32}Mg beam selection

The ^{32}Mg secondary beam was selected by the A1900 mass spectrometer, as described in Section 3.1.2. The beam was 95% pure with the main contaminant being ^{34}Al , which accounted for 1.5% of the beam. Light fragments produced in the A1900 wedge were also present at a rate of 1.7%. Separation in the A1900 was accomplished by variations in the mass-to-charge (m/q) ratio of the components of the beam.

The m/q ratios of the beam and the contaminants are given in Table 4.2. The velocities of the different components were calculated from the magnetic rigidity, $B\rho$, of the final segment of the A1900 of 3.6416 Tm. The distance from the A1900 object scintillator to the target timing scintillator was 11.52 m, which allowed the time-of-flight from the A1900 object scintillator to the timing scintillator just upstream from the reaction target to be calculated, shown in Table 4.2. The separation in time-of-flight of the three beam species listed in Table 4.2 indicates that separation of the ^{32}Mg beam from contaminants was possible. The ^{32}Mg beam particles were individually selected from the contaminants using this time-of-

Table 4.2: Tabulation of the calculated mass-to-charge ratios, velocity of beam fragments, and time-of-flight from A1900 to the timing scintillator for the secondary beam, ^{32}Mg , and the major contaminants.

Beam	mass-to-charge ratio (m/q)	velocity (v)	ToF A1900-timing scint
^{32}Mg	$32/12 = 2.667$	13.66 cm/ns	84.33 ns
^{34}Al	$34/13 = 2.615$	13.92 cm/ns	82.74 ns
^{30}Na	$30/11 = 2.727$	13.35 cm/ns	86.28 ns

flight and the charge deposited in the timing scintillator, as indicated in Figure 4.3.

4.3.2 Element identification

Identification of the atomic number of each fragment was accomplished using a two-dimensional representation of the energy-loss versus total energy, with the energy loss taken as the ΔE from the ion chamber and residual energy from the thick scintillator signal. The quality of the elemental separation for all Sweeper settings is shown in Figure 4.4. ΔE versus E_{tot} can be used to identify the atomic charge (Z) since

$$\Delta E = \Delta x \times \frac{dE}{dx} \propto \frac{mZ^2}{E} \quad (4.4)$$

where m and E are the ion's mass and energy, respectively and x is the thickness of the material.

The unreacted beam is the strongest component in these distributions, which clearly identifies the $Z=12$ magnesium events. The resolution is adequate to clearly separate the $Z=10$ neon isotopes from the surrounding $Z=11$ sodium and $Z=9$ fluorine fragments. Gates were applied to these spectra to select the isotopes for further analysis.

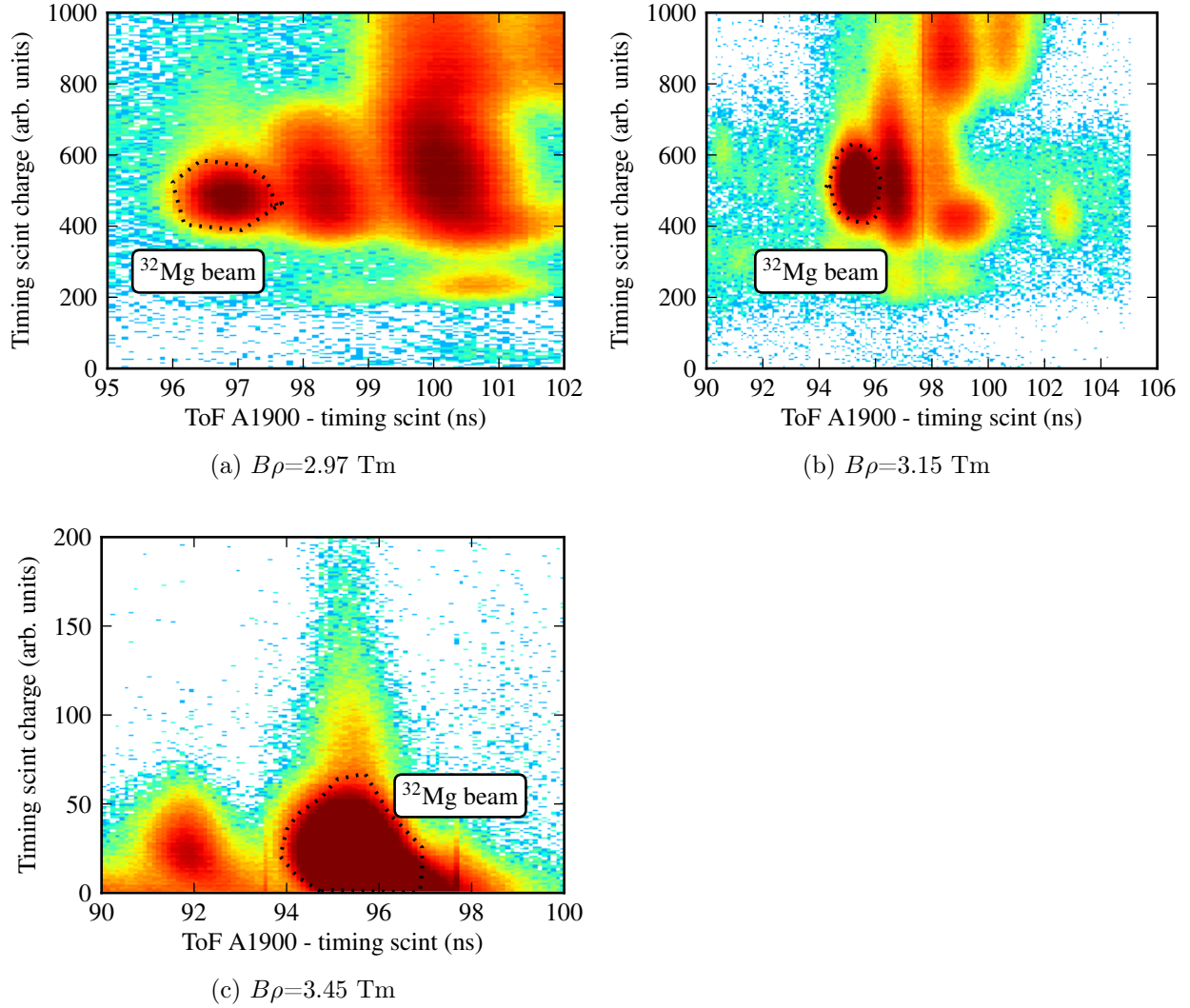


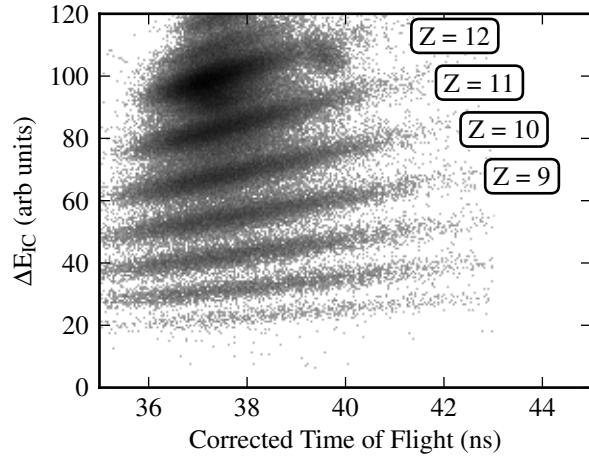
Figure 4.3: Beam identification plots using charge deposited in the scintillator upstream of the target versus ToF from the A1900 object plane to the timing scintillator in the vault.

4.3.3 Isotope separation

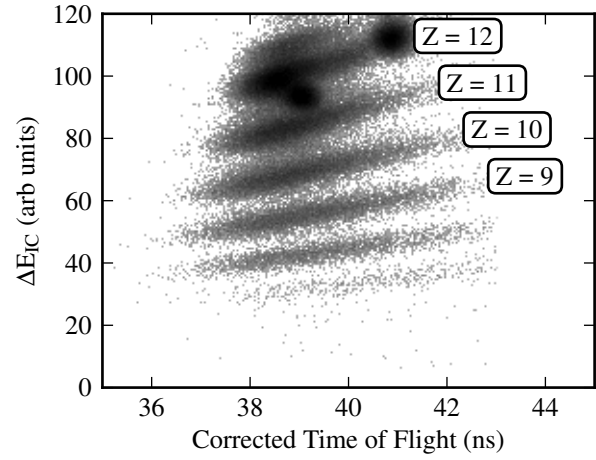
The Sweeper dipole magnet disperses isotopes by their momentum-to-charge ($\frac{|p|}{q}$) ratio, according to the magnetic rigidity ($B\rho$) of the magnet:

$$\rho = \frac{|p|}{qB} = \frac{|v|m}{qB} \quad (4.5)$$

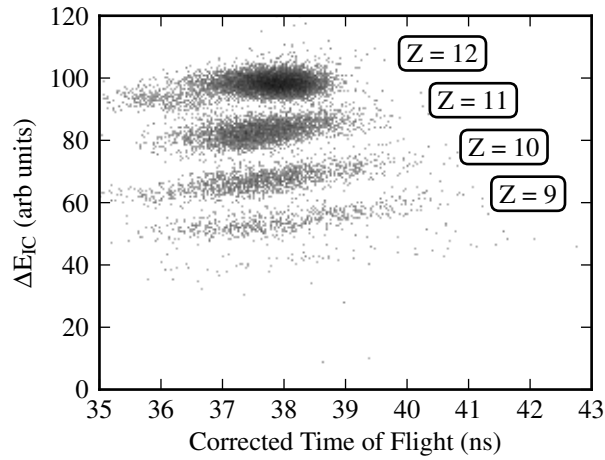
This dispersion causes differences in the path lengths of the fragments that pass through the Sweeper magnet. If velocity in the above expression is replaced by distance (D) over time



(a) 2.97 Tm



(b) 3.15 Tm



(c) 3.45 Tm

Figure 4.4: Energy loss signals from the ion chamber as a function of the ToF from the scintillator upstream of the target to the thin scintillator downstream of the Sweeper magnet. Elemental separation is shown for the three Sweeper rigidity settings used in this work: (a) 2.97 Tm, (b) 3.15 Tm, (c) 3.45 Tm.

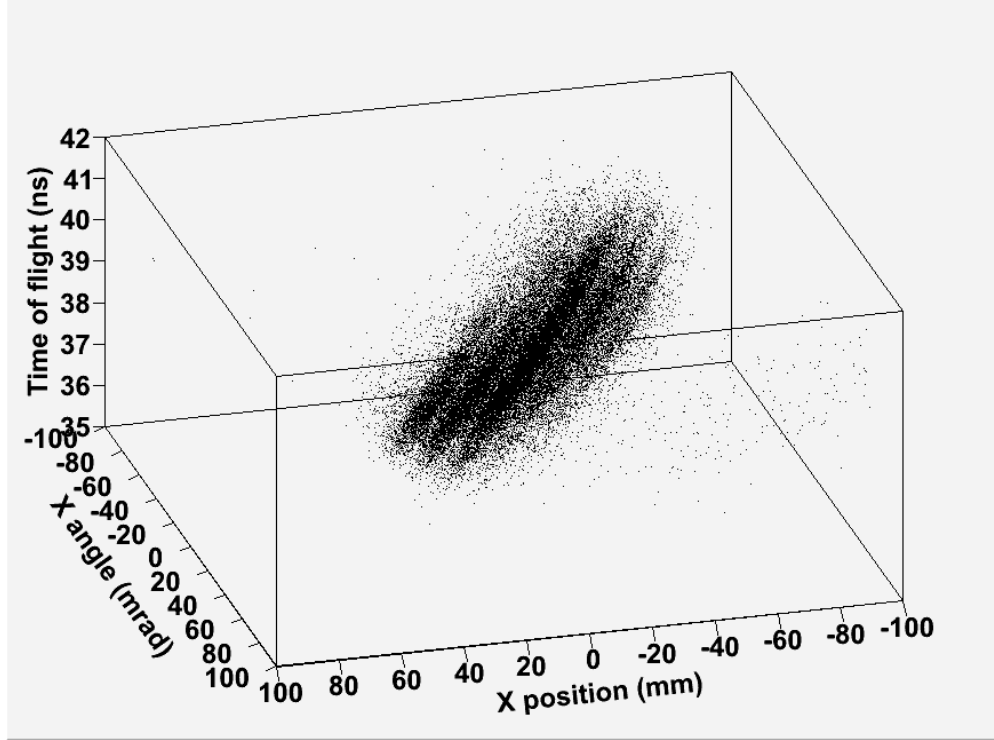


Figure 4.5: 3-d histogram of x-position vs x-angle vs time-of-flight observed for Ne isotopes with the 3.15 Tm setting of the Sweeper magnet.

(t), then the following expressions result:

$$\frac{D}{t} = \frac{qB\rho}{m} \quad (4.6)$$

or

$$t = \frac{Dm}{qB\rho} \quad (4.7)$$

Thus, the time-of-flight for fragments that pass through the Sweeper magnet is directly proportional to the path length (D), which allows for a separation in time according to the mass-to-charge ratio of the fragment. The situation is complicated by variations in the incoming trajectories of the particles and the spread in the momentum distribution resulting from the reaction, both of which introduce a correlation between the position and angle of the fragments in the detectors. A corrected time-of-flight was calculated with tracking information from the CRDCs, according to the method described in detail in Ref. [40].

The isotope separation of neon fragments can be seen in the 3-dimensional histogram of

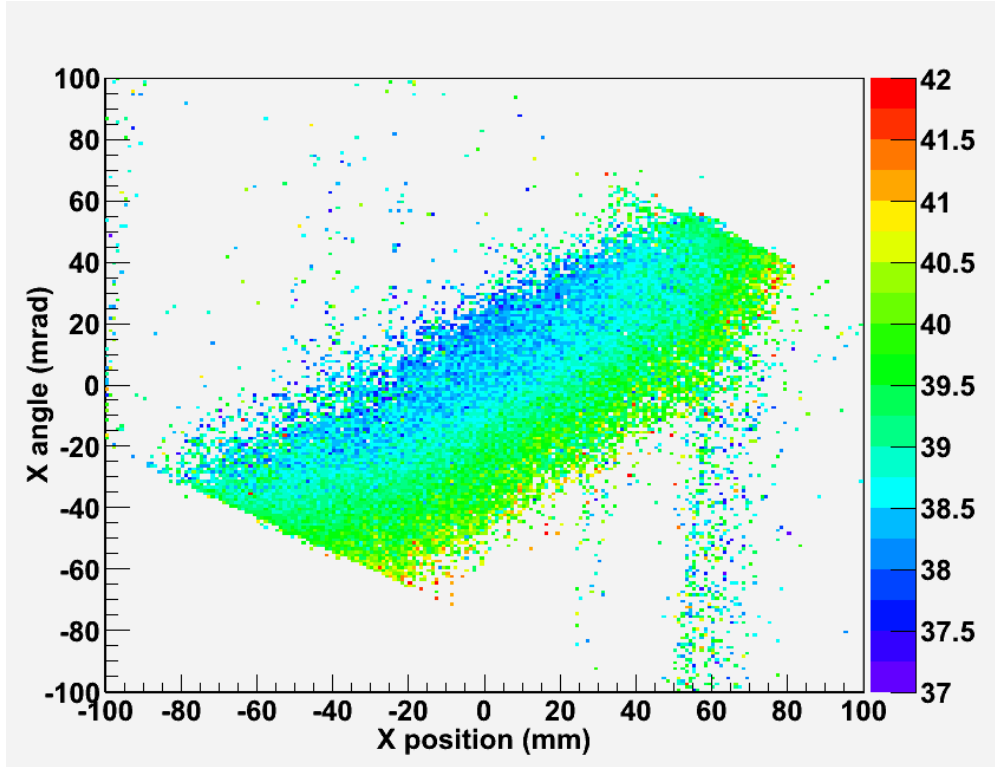


Figure 4.6: Projection of the time-of-flight shown in Figure 4.5 onto the x-position vs. x-angle plane. Colors represent the time-of-flight. Bands of constant color were used to construct a corrected time-of-flight parameter

the x-position versus x-angle versus time-of-flight shown in Figure 4.5. The bands in this figure represent the different isotopes of neon. The correlation between the position and angle must be reduced into a single parameter to create a corrected time-of-flight. This was accomplished by the projection of the three-dimensional histogram onto the position-angle plane, the result of which can be seen in Figure 4.6. The bands of constant color represent constant time-of-flight through the Sweeper system. A second order polynomial was used to describe the curvature of these bands and to produce a linear variation referred to as “emittance”. The polynomial parameters are given in Tables 4.3, 4.4, and 4.5. The variation of the emittance parameter is shown versus time-of-flight in Figure 4.7, where isotope separation is now depicted in two dimensions. The correlation between emittance and time-of-flight was then removed by a linearization to produce a corrected time-of-flight.

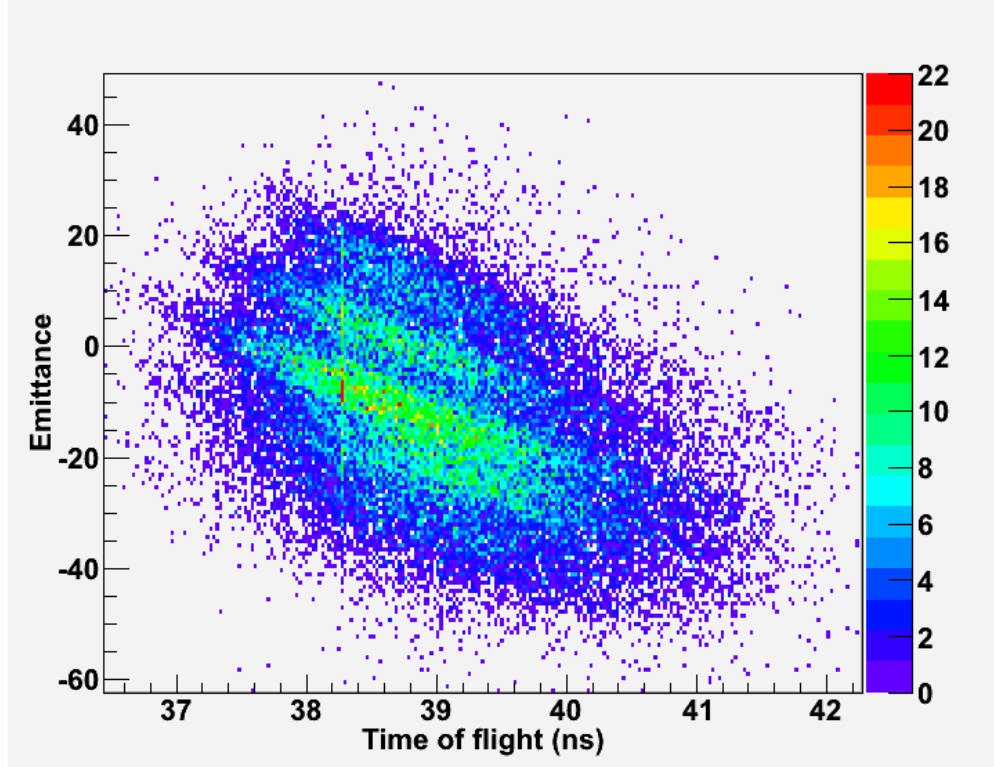


Figure 4.7: “Emittance” versus corrected time of flight for the neon data obtained with the 3.15 Tm magnet setting, resulting from the projection of the data shown in Figure 4.6

Further corrections were applied to account for other dependencies observed in the focal plane detectors. Tables of the correction parameters for all three Sweeper settings can be seen in Tables 4.3, 4.4, and 4.5. The overall separation obtained for neon, sodium, and fluorine isotopes is shown in Figure 4.8. Excellent separation was obtained for all these products at the two lower magnetic field settings. Poor resolution in the timing scintillator, caused by its operation in the Sweeper magnet fringe field, meant that only the neon isotopes could be reliably separated at the highest magnetic rigidity.

4.4 Fragment production cross section

Yields for charged fragments were compared to those predicted by LISE++ [6] for charged fragments with complete momentum distributions in the focal plane of the Sweeper magnet.

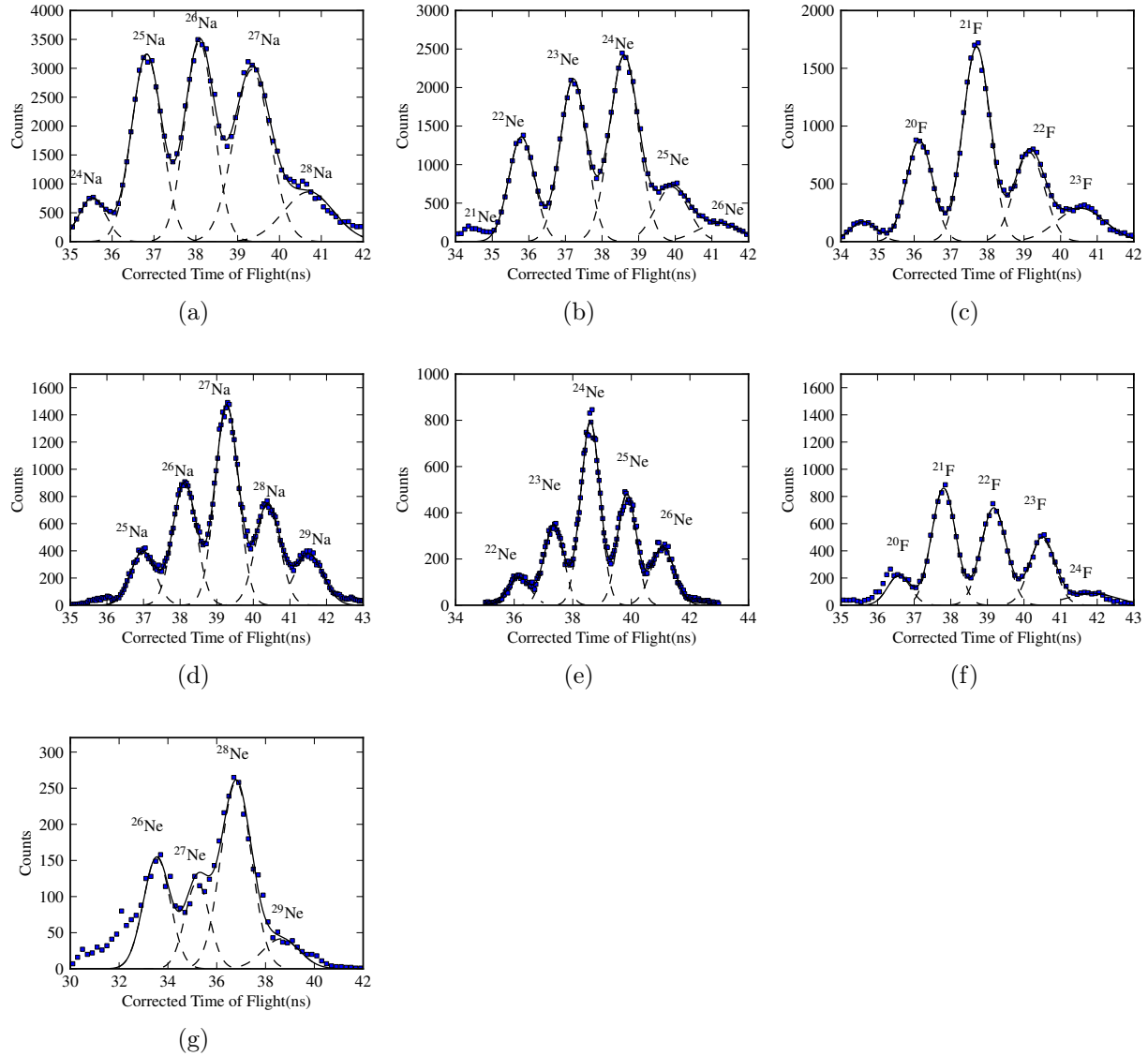


Figure 4.8: Particle identification functions for the observed isotopes for sodium (4.8a), neon (4.8b), and fluorine (4.8c) from the 2.97 Tm setting, sodium (4.8d), neon (4.8e), and fluorine (4.8f) from the 3.15 Tm setting, and neon (4.8g) from the 3.75 Tm setting.

Table 4.3: Time-of-flight correction parameters for the 3.15 Tm setting. Polynomial order was determined empirically.

Parameter	First order	Second order
Emittance	0.10156	–
Y position	-0.00873	-0.0004237
X position	0.000794	-0.000309
Thick scint energy	0.001233	–
CRDC y position	0.00487	5.98e-5

Table 4.4: Time-of-flight correction parameters for the 3.75 Tm setting

Parameter	First order	Second order
Emittance	0.160	–

Table 4.5: Time-of-flight correction parameters for the 2.97 Tm setting

Parameter	First order	Second order
Emittance	0.11299	–
Y-position	0.004443	0.0004776
Y-angle	0.00576	0.0015
Thick energy	0.00159	–

The large momentum distributions for these fragments and wide range of charged fragments observed meant that only a few of the many observed fragments were centered on the focal plane with complete distributions. The tabulation of these cross sections is shown in Table 4.6. The comparison between the observed and simulated cross sections indicates that there is a trend of under prediction in the cross section in LISE, but agreement is within 1σ .

4.5 Neutron hits

When a beam particle passed through the target scintillator, a coincidence window was opened to record neutron hits in MoNA/MoNA'. As described in Section 3.2.6, a hit in

Table 4.6: Comparison of observed experimental production cross sections for centered charged fragments with LISE++ predictions

Fragment	Experimental cross section (mb)	LISE++ cross section (mb)
^{26}Na	14 ± 3.5	10.8
^{27}Na	23 ± 6	17.6
^{24}Ne	14.5 ± 4	10

MoNA/MoNA' was considered valid when both PMTs on a single bar registered a signal above the threshold. The number of neutrons emitted in the reaction could not be directly measured as a result of neutrons scattering on carbon nuclei in the scintillator (so called dark scattering) and multiple scattering of neutrons within the array.

Though the number of hits in MoNA/MoNA' does not directly measure the true multiplicity, meaning the number of neutrons emitted in the reaction, the simple hit multiplicity, the number of valid neutron events, should increase as the number of emitted neutrons increases. This increase was confirmed with GEANT4 simulation of the detector response. The hit multiplicity was defined as the number of bars in MoNA/MoNA' in which both PMTs see a signal with amplitude greater than the hardware threshold of 10 mV (350 keVee). The neutron hit multiplicity distribution was a compilation of all neutron information for a given fragment, binned according to the number of bars with a valid signal on an event-by-event basis. The neutron hit multiplicity distribution was used in the subsequent analysis to determine the best-fit precursor fragment and excitation energy for each observed fragment. The distributions are shown in Figures 5.1, 5.2, and 5.3. The distributions are shown in terms of "Probability", where the distributions were normalized relative to the total number of observed hits for each fragment.

The kinetic energy of forward-directed neutrons was used to verify the source of the neutrons. Neutrons emitted by de-excitation of the precursor projectile fragment should have a kinetic energy similar to that of the beam, roughly 80 MeV. In contrast, neutrons stripped from the projectile by the target should have a kinetic energy roughly half that of

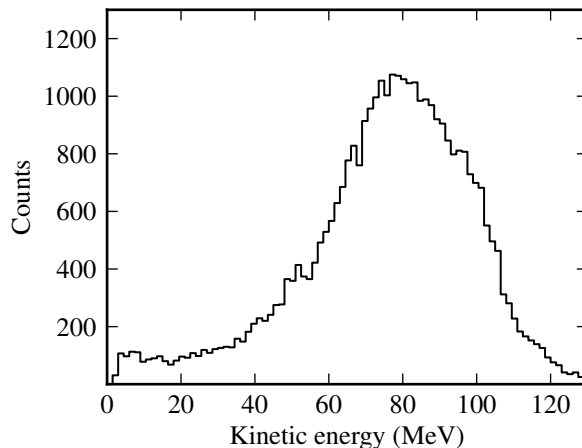


Figure 4.9: Neutron kinetic energy from MoNA/MoNA' for a ^{25}Ne final fragment.

the beam, since nucleon removal from the projectile is a nucleon-nucleon process. Thus, the kinetic energy of the removed neutron should be equal to the energy of the center-of-mass. As the target is stationary, of course, the neutron energy should be reduced by half.

The kinetic energy spectrum of observed, forward-focused neutrons in MoNA/MoNA' during this experiment is shown in Figure 4.9. The distribution is roughly Gaussian, with a slight asymmetry towards smaller energies. The slight skew in the distribution indicates that a small portion of the detected neutrons were generated by direct interaction with the target, rather than the subsequent de-excitation process.

Chapter 5

RESULTS

The neutron hit multiplicity distributions from the MoNA/MoNA' arrays were compared to the output from a statistical evaporation model that was passed through a filter for the detector response. Following a χ^2_{ν} analysis, the best prefragment and excitation energy were determined for each observed particle. The excitation energy was found to increase with total mass loss, $A_b - A_f$, with a wide range of excitation energies produced for a given fast-step mass loss, $A_b - A_f^*$. The variation in excitation energy with mass loss was then compared to the previous model predictions.

5.1 Detector modelling

The GEANT4 code was used to model the present experiment to determine the neutron coincidence probability [41]. The simulation included the Sweeper magnet steel and the neutron detector bars that were composed of carbon and hydrogen with light guides and PMTs to simulate full detector response. The neutron interaction cross sections were taken from the Menate_R package [42]. However, the Menate_R package included only neutron interaction cross sections for carbon and hydrogen. The wide angular coverage of MoNA/MoNA' for this experiment required that interactions with the steel in the Sweeper magnet be included in the simulation. Thus, the addition of neutron scattering cross sections with iron was crucial to successfully model detector response. Experimental cross sections for all neutron interactions in the relevant energy region with iron were taken from Ref. [43] and added to the simulation [44].

The GEANT4 simulation was given input from a text file in a specified format (pythia) giving the particle type (in this case neutrons), the momentum vector in the laboratory frame and the mass energy of the particle. The detector response of neutrons produced by an

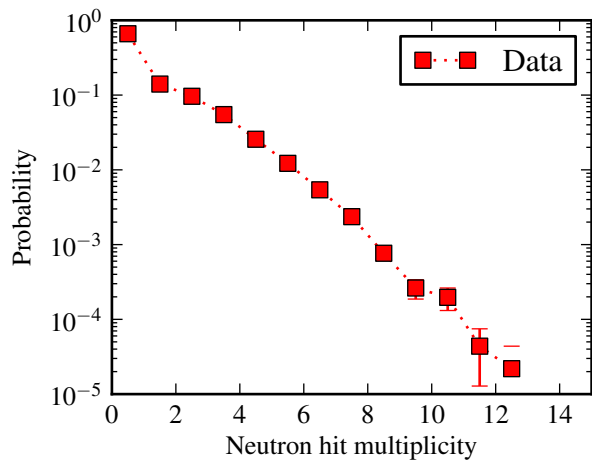
evaporation model was then obtained for each intermediate fragment and excitation energy and compared directly to the experimentally observed neutron hit multiplicity distribution.

5.2 Neutron evaporation simulation

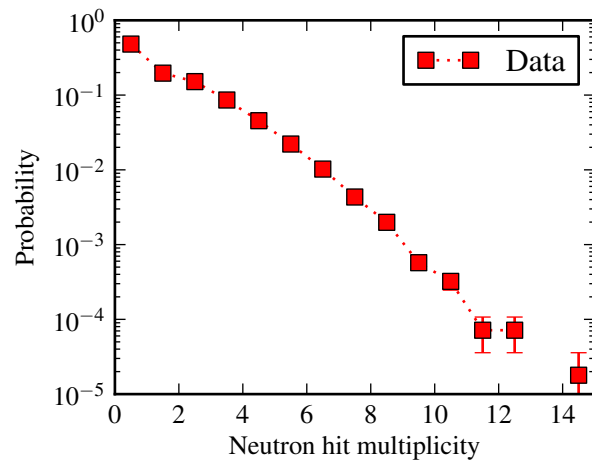
After the initial fragmentation process, the precursor fragment was assumed to be formed in an excited state that de-excites by the emission of particles and gamma rays. The statistical evaporation code PACE [17], described in detail in Section 2.3, was used to simulate this process. A PACE calculation could only be performed for a single nucleus at a single, discrete excitation energy. To explore the neutron evaporation products from all prefragments and energies, this decay calculation was carried out for a wide range of prefragments in 1 MeV steps of excitation energy. The energy and momentum information for the evaporated neutrons was then coupled to the assumed prefragment momentum to boost the simulated neutrons into the lab frame. The detector response to each evaporation neutron was then simulated using GEANT4, described in section 5.1. The evaporation neutrons were considered on an event-by-event basis in GEANT4.

The individual results of this simulation from each PACE monte carlo event were then combined and compared to the observed neutron multiplicity distribution for each final fragment. The measured neutron hit multiplicity distributions are shown in Figures 5.1, 5.2, and 5.3 for all of the fragments observed in this work. An example hit multiplicity distribution with a comparison to the results from the PACE/GEANT4 simulation is provided in Figure 5.4. As was previously mentioned, a discrete energy was required for each evaporation simulation. The simulation results shown in Figure 5.4 represented the energy minimum for each prefragment determined by the χ^2_{ν} minimization technique discussed below.

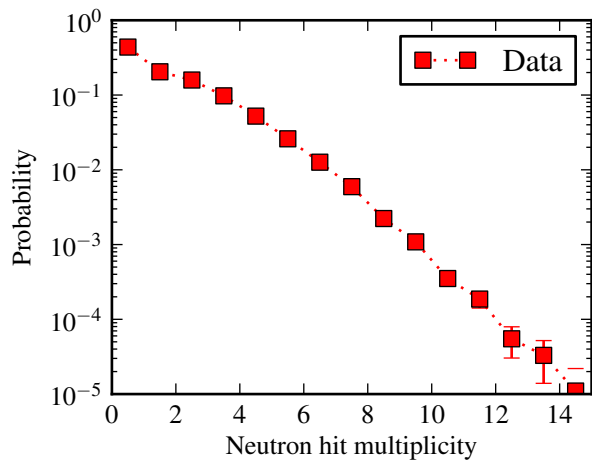
The total hit multiplicity from each simulation, determined from a sum of the hit multiplicity from the MoNA and MoNA' detectors, was then compared to the experimental hit multiplicity for each fragment. The figure of merit for comparing each prefragment and excitation energy from the simulation to the experimental data was established with a χ^2_{ν}



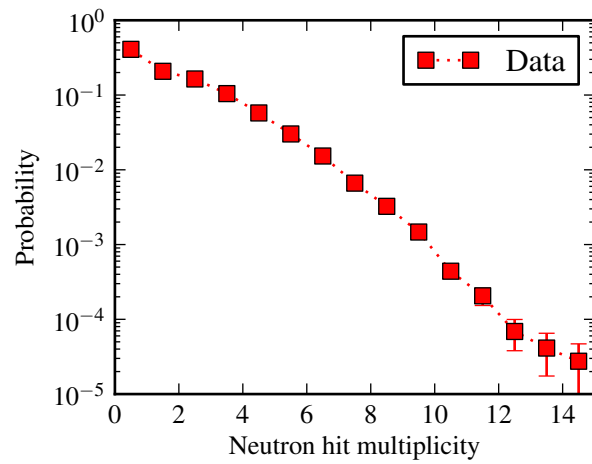
(a)



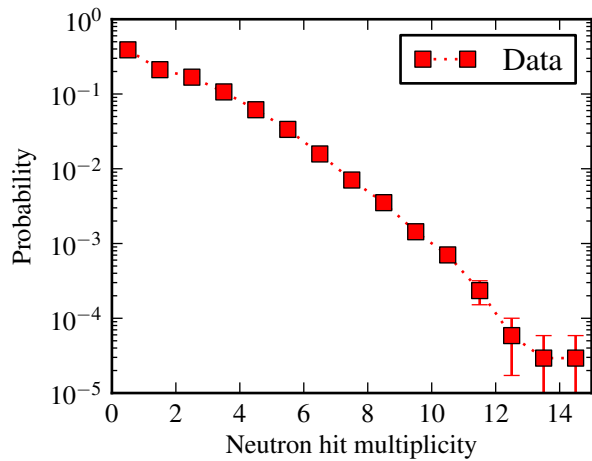
(b)



(c)

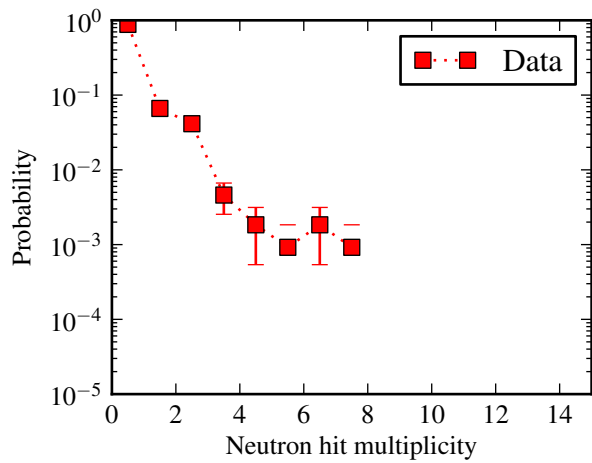


(d)

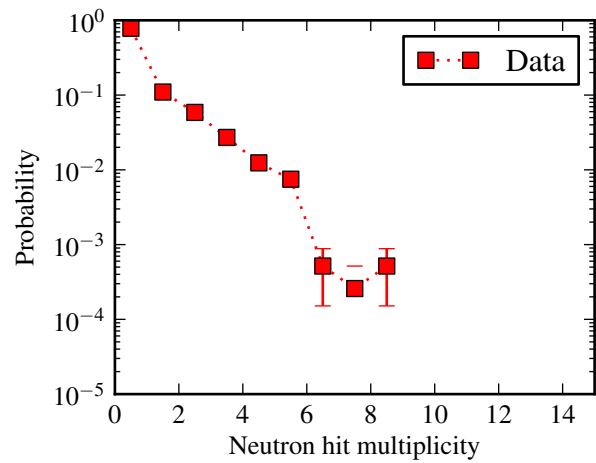


(e)

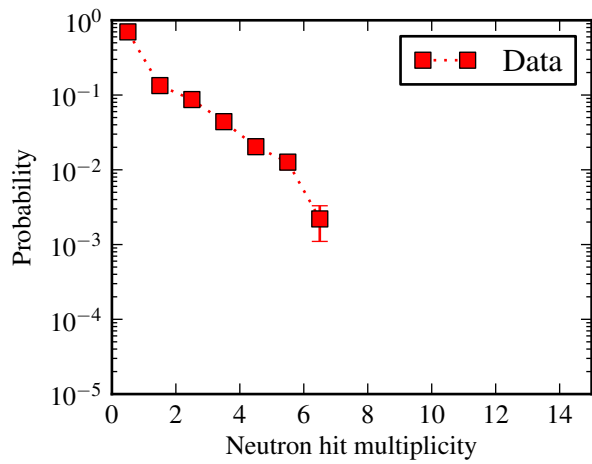
Figure 5.1: Neutron hit multiplicity data for the observed sodium fragments (^{29}Na (5.1a) - ^{25}Na (5.1e))



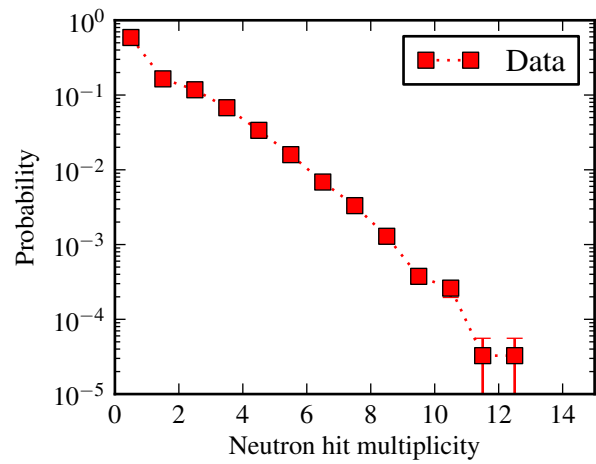
(a)



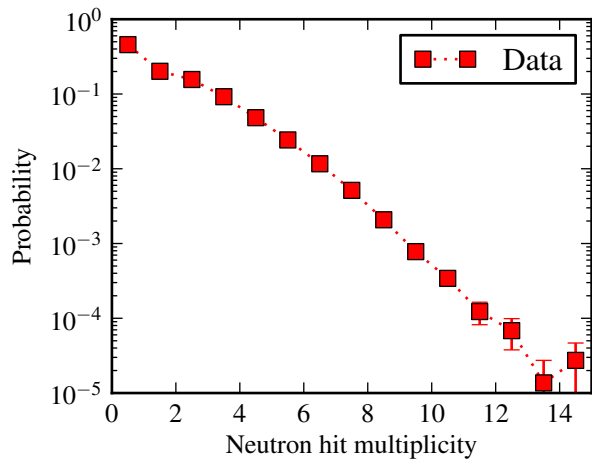
(b)



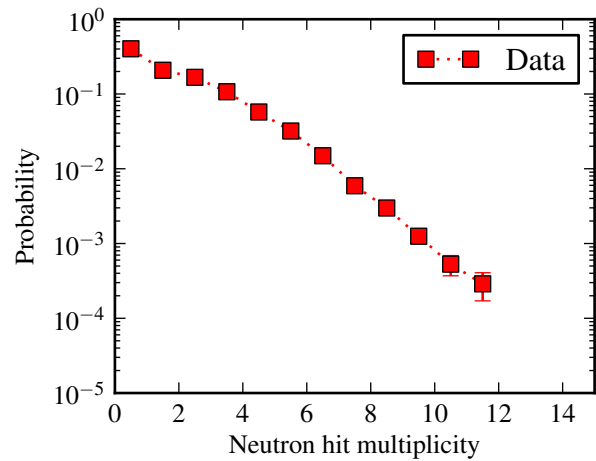
(c)



(d)



(e)



(f)

Figure 5.2: Neutron hit multiplicity data for the observed neon fragments (^{29}Ne (5.2a) - ^{24}Ne (5.2f))

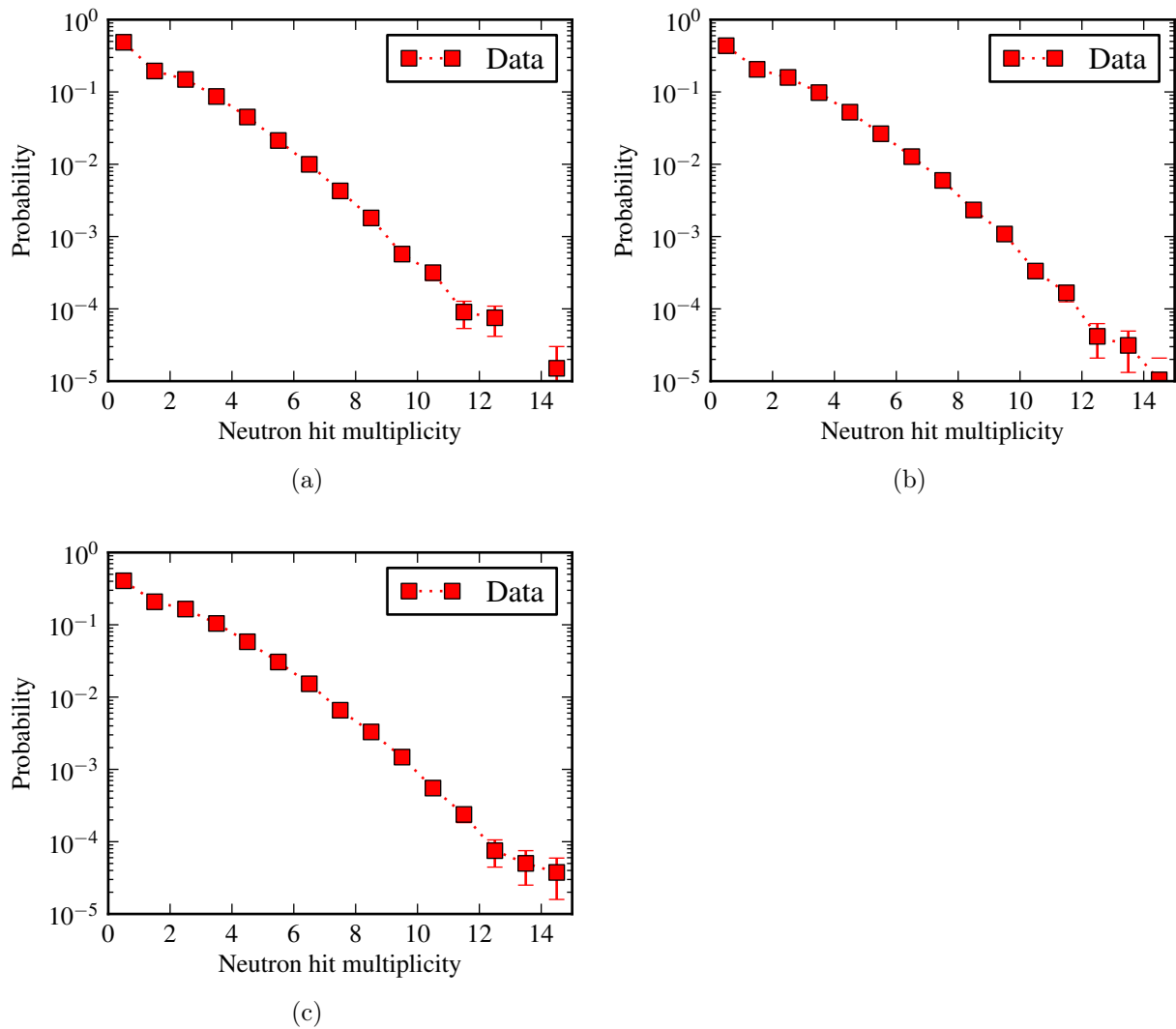


Figure 5.3: Neutron hit multiplicity data for the observed fluorine fragments (^{23}F (5.3a) - ^{21}F (5.3c))

analysis. The quality of fit was determined by comparison of the binned experimental data to the binned simulation output by the following statistic:

$$\chi^2 = \sum_i \frac{(D_i - S_i)^2}{D_i + S_i} \quad (5.1)$$

and

$$\chi^2_\nu = \frac{\chi^2}{\text{ndf}}, \quad (5.2)$$

where i is the bin number (multiplicity value) in the histogram, D_i is the experimental value of the multiplicity, S_i is the value from the simulation, and ndf is the degrees of freedom [45].

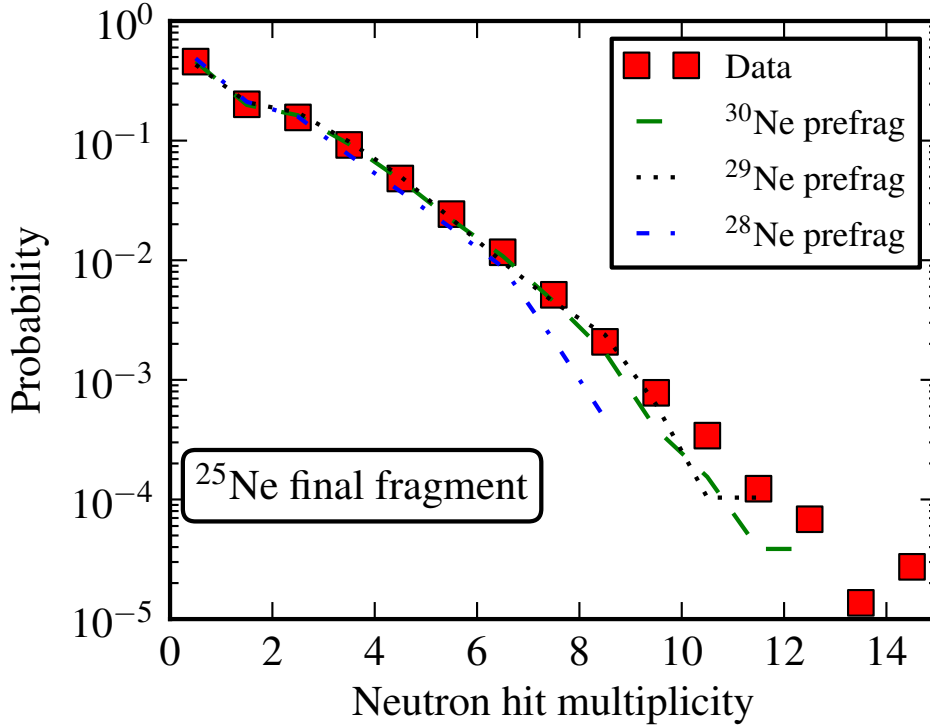


Figure 5.4: Comparison of the experimental hit multiplicity with the results of the PACE/GEANT4 simulation for ^{25}Ne final fragments. The hit multiplicity distributions from the assumed ^{30}Ne , ^{29}Ne , and ^{28}Ne prefragments at the “best” excitation energies of 43, 23, and 14 MeV respectively, are shown.

These χ^2_ν values were then used to generate, for each final fragment, a set of curves, which showed the variation of the precursor mass and excitation energy from simulation. The curves for all final fragments are shown in Figures 5.5, 5.6, and 5.7. These χ^2_ν curves were used to extract the best E^* and A^* for each observed final fragment. It should be noted that there are some constraints on the prefragment formation and de-excitation process. First, PACE calculations showed that charged particle evaporation was strongly suppressed in these nuclei. Therefore, all prefragments should have the same atomic number as the product. Also, the pickup of neutrons by the projectile from the target was assumed to be very small [3]. Thus, the heaviest prefragment for the neon isotopes was taken to be ^{30}Ne , since neon has two fewer protons than the magnesium. Similar arguments were applied to the other elemental data analyzed in this work. The absolute minimum in χ^2_ν for the fluorine

isotopes shows a smaller difference from the other local minima. The small changes in χ_{ν}^2 minima for fluorine indicates that the simple picture of a single precursor fragment forming the final fragment may not be valid for fluorine products.

The ^{29}Ne final fragment offers a straightforward examination of the prefragment as the only reasonable reaction sequence is $^{32}\text{Mg} \rightarrow ^{30}\text{Ne}^* \rightarrow ^{29}\text{Ne}$. The χ_{ν}^2 minimum depicted in Figure 5.6a is therefore the best fit. For a more complex case, such as ^{25}Ne , which is seven nucleons removed from the ^{32}Mg beam, several neon prefragments are possible. The χ_{ν}^2 distribution for each prefragment displays a minimum excitation energy, with $^{30}\text{Ne}^*$ showing the best overall fit at 43 MeV as shown in Figure 5.6e. Higher mass fragments were not considered to be possible as discussed above.

A direct measure of the total nucleon loss, $A_b - A_f$, between the ^{32}Mg beam and the final fragments detected in the Sweeper magnet focal plane was possible from these measurements (see Fig. 5.8). The excitation energies extracted from the χ_{ν}^2 analysis of the neutron hit multiplicity distributions from experiment and PACE/GEANT4 simulation are shown for this observable in Figure 5.9. In general, an increase of excitation energy with total mass loss is observed but with some variation as a function of atomic number. Such variation is not predicted by the abrasion models.

5.3 Reaction precursor fragments

The variation of the extracted excitation energy with the total change in mass number, $\Delta A = A_b - A_f$ (see Figure 5.8), was found to be linear with slopes of approximately 11, 8, and 17 MeV/ ΔA , respectively. The fact that the slopes depend on the atomic number of the product indicates a variation in excitation energy with the number of protons removed in the first step of the reaction. As mentioned above, the statistical evaporation calculations completed as part of this work indicated that proton evaporation is minimal for these neutron-rich systems. Note that this observable combines mass loss for the entire reaction. On the other hand, the variation of excitation energy with mass loss in the first

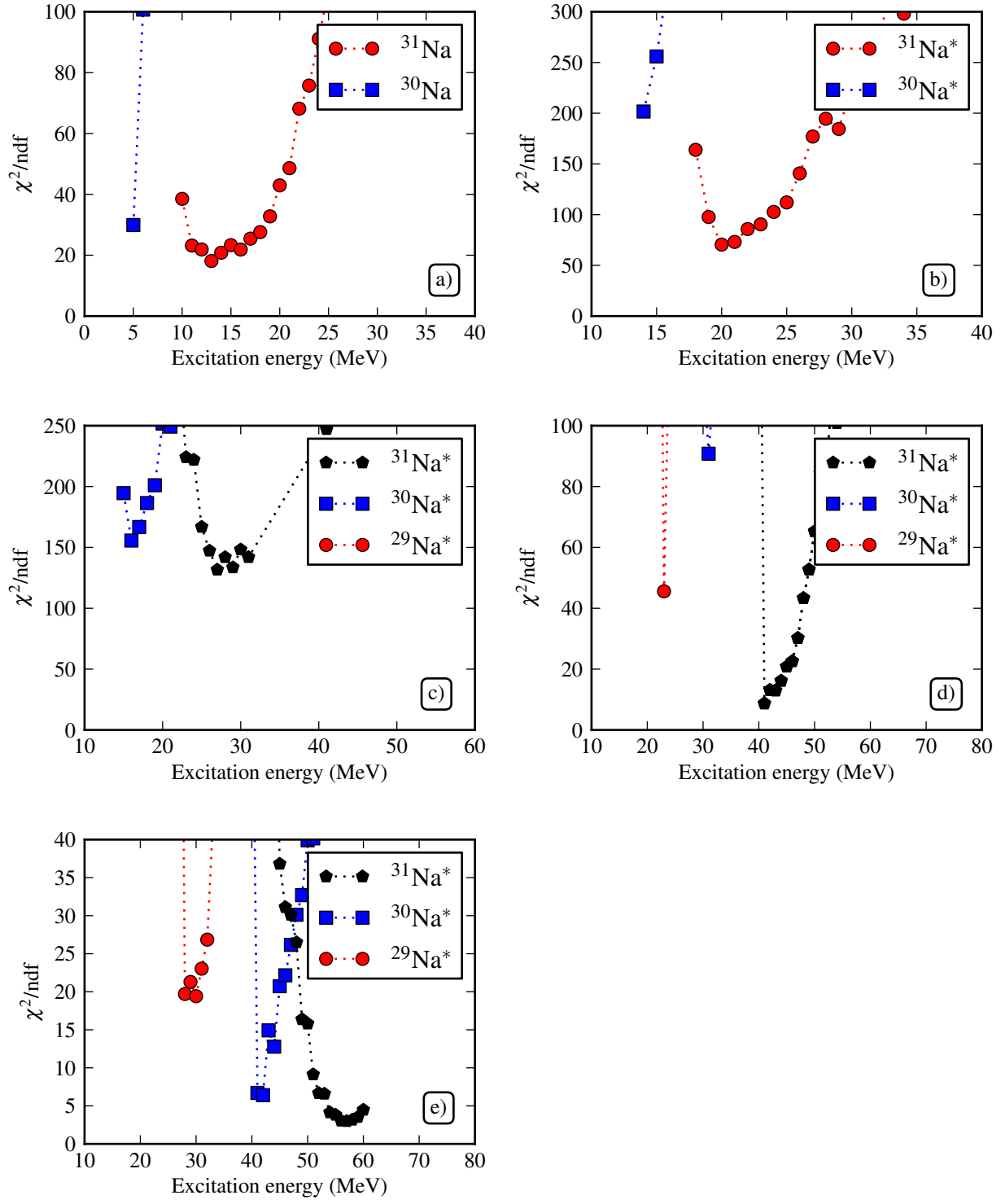


Figure 5.5: The reduced χ^2_{ν} surface obtained for the observed sodium fragments, see the text for an explanation. Observed fragments were 5.5a ^{29}Na , 5.5b ^{28}Na , 5.5c ^{27}Na , 5.5d ^{26}Na , and 5.5e ^{25}Na .

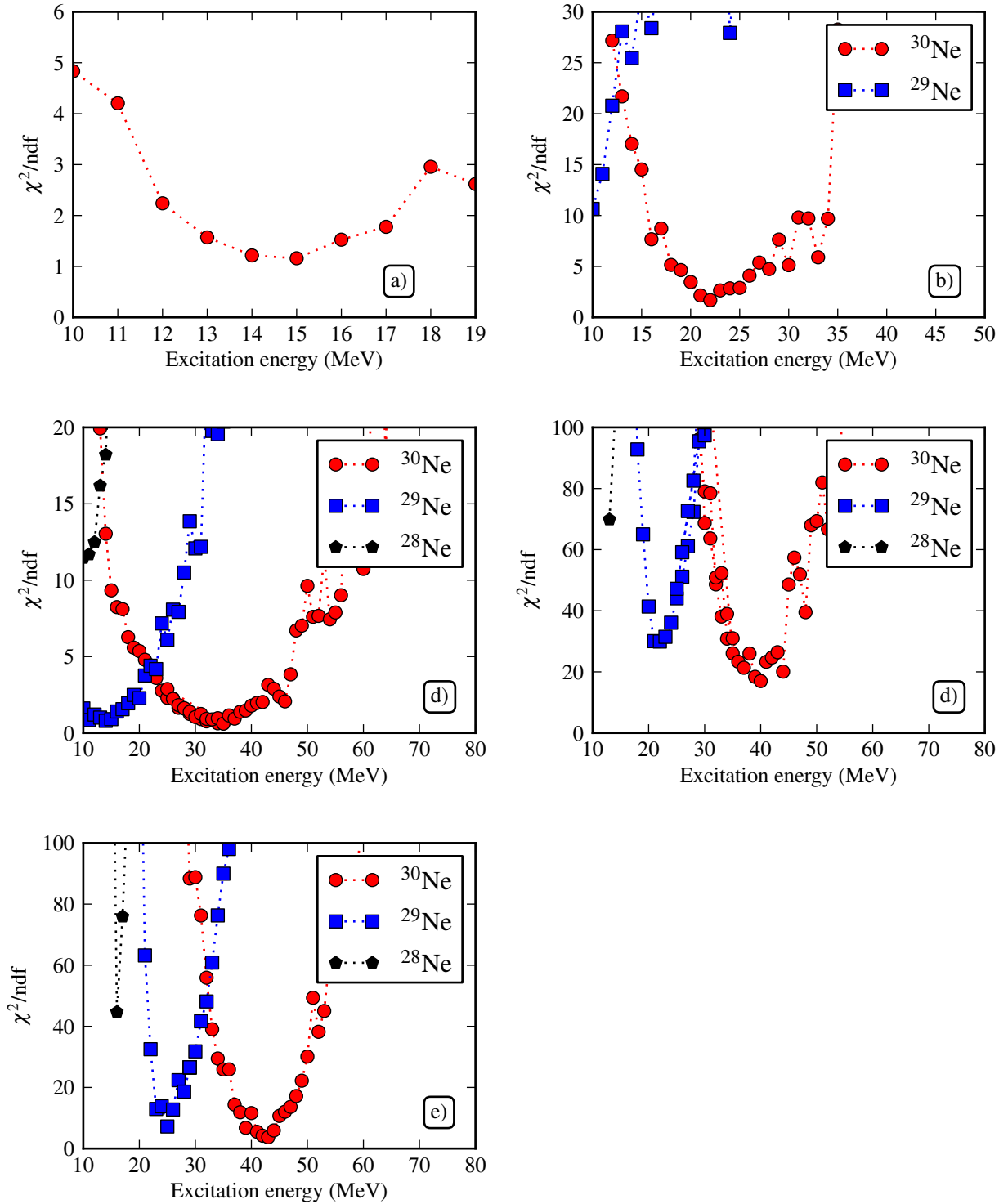


Figure 5.6: The reduced χ^2_{ν} surface obtained for the observed neon fragments, see the text for an explanation. Observed fragments were 5.6a ^{29}Ne , 5.6b ^{28}Ne , 5.6c ^{27}Ne , 5.6d ^{26}Ne , and 5.6e ^{25}Ne .

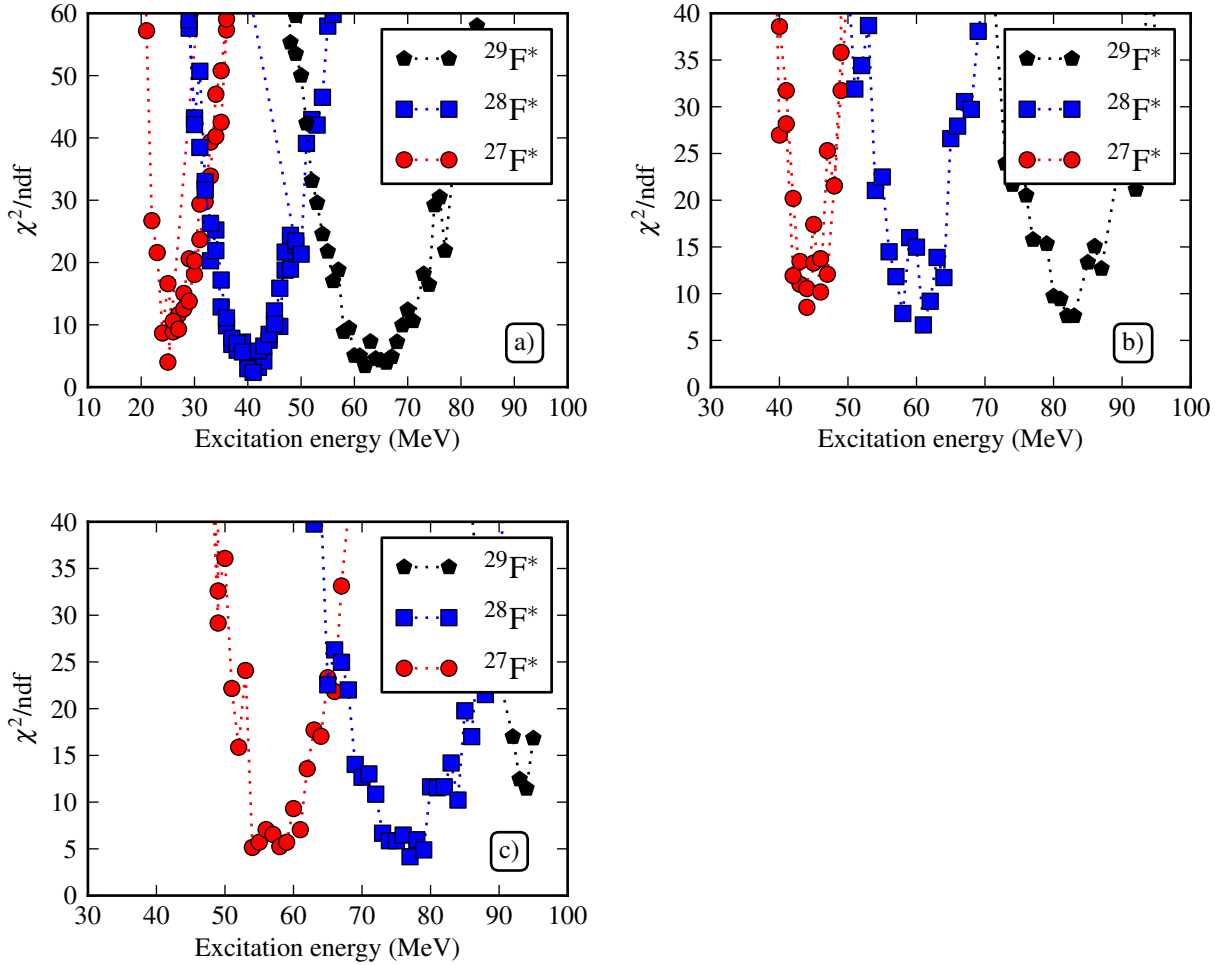


Figure 5.7: The reduced χ^2_{ν} surface obtained for the observed fluorine fragments, see the text for an explanation. Observed fragments were 5.7a ^{23}F , 5.7b ^{22}F , and 5.7c ^{21}F .

step, $\Delta A^* = A_b - A_f^*$, is the quantity that is predicted by various models of the reaction. The new result in this work is an estimate of the mass of the precursor mass fragment, A_f^* . The value of A_f^* for each observed fragment was taken as the mass number of the precursor fragment with the lowest χ^2_{ν} in the neutron hit multiplicity analysis described in Section 5.2. The resulting distribution of excitation energy in the precursor fragment and mass removal in the first step of the reaction are shown in Figure 5.9. The results suggest a remarkable situation of relatively small mass-loss in the first step of the reaction with the creation of a large range of high excitation energies that lead to multi-neutron emission. For example, the neon fragments were found to be consistent with evaporation of up to six neutrons from

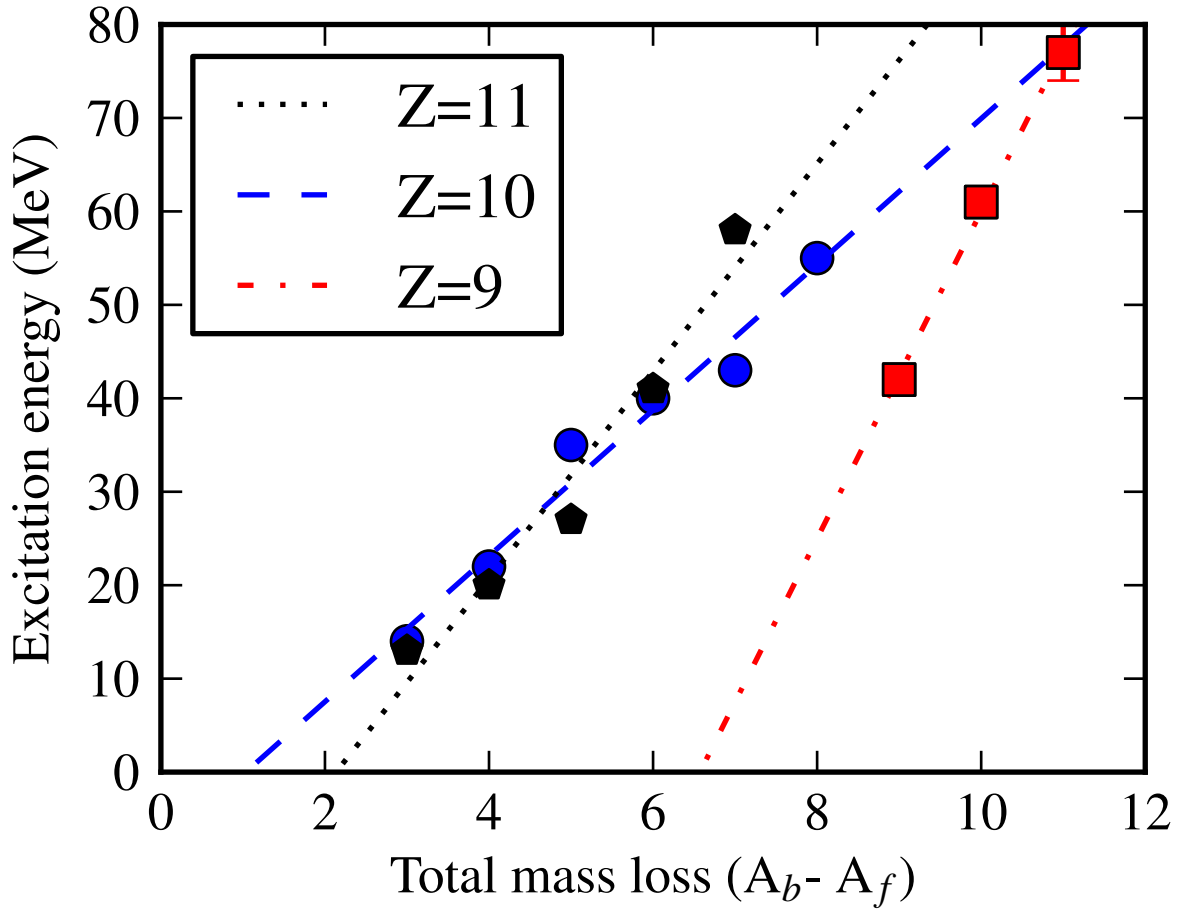


Figure 5.8: Excitation energy (E^*) obtained from the χ^2_ν analysis versus total mass loss ($\Delta A = A_i - A_f$) for the observed isotopes with linear fits to the data.

the single precursor mass, $A=30$.

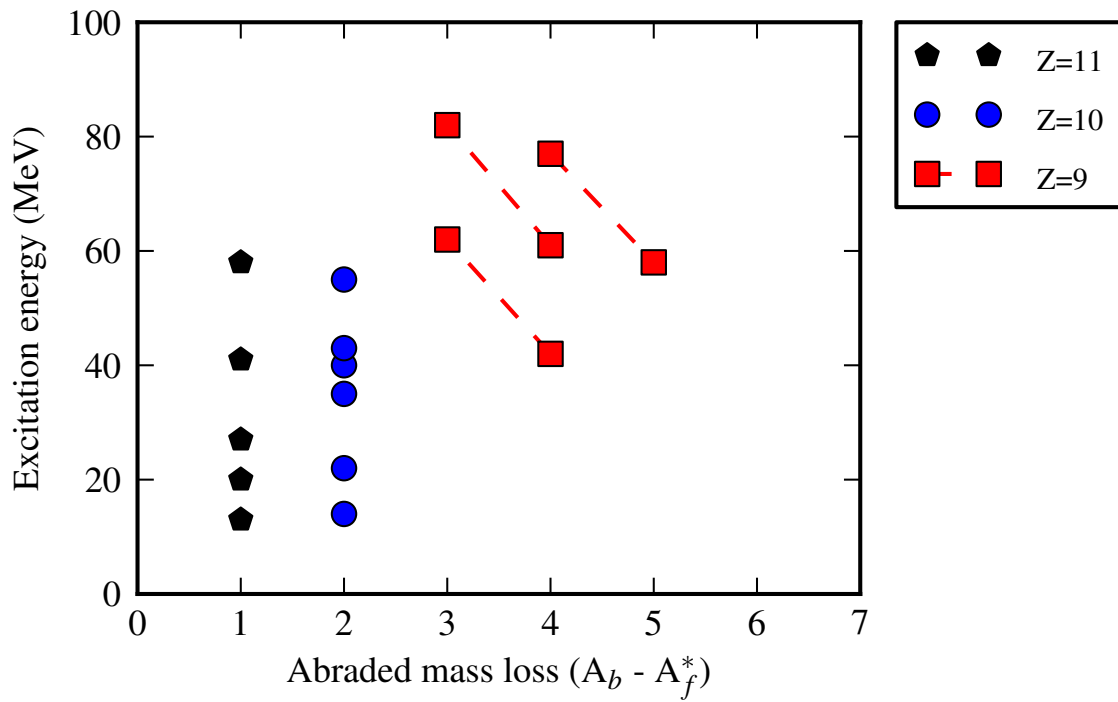


Figure 5.9: Excitation energy (E^*) versus mass loss in the fast reaction step ($A_b - A_f^*$). Two points (connected by a dashed line) are shown for each observed fluorine isotope, as the difference between χ^2_{ν} minima for the simulated prefragments is small.

Chapter 6

COMPARISON TO REACTION MODEL

Examples of the theoretical predictions of the excitation energy, E^* , as a function of mass loss in the first step, $A_b - A_f^*$, are compared to the present results in Figure 6.1. The abrasion/ablation models show a simple correlation of mass loss and excitation energy that is not supported by the data. Wilson et al. [24] combined the contribution of the excess surface energy and rescattering of the participant nucleons in the bulk material that resulted in an excitation energy of roughly 3.3 MeV per nucleon removed in the abrasion step. The energies predicted by Wilson et al. are below those energies observed in this work. Gaimard and Schmidt [25] used a microscopic description that produces the excitation energy by the removal of nucleons bound in a mean-field potential, giving 13.3 MeV per removed nucleon. The magnitude of the energies predicted by Gaimard et al. is greater than Wilson et al., but the same general increase in excitation energy with abraded mass loss is predicted. For both abrasion/ablation models, a narrow range of excitation energies is predicted for a given mass loss, $A_b - A_f^*$. The narrow band of excitation energies is not supported by the results of the present work.

On the other hand, the internuclear cascade model [26], [27] describes a range of excitation energies at small mass losses. Excitation energy distributions from $Z=11$ (sodium) precursors can be seen, for example, in Figure 6.2. This range of excitation energies is much more consistent with the present results. The production cross sections for precursor fragments decrease with increased mass loss from the beam ($A_b - A_f^*$), as presented in Figure 6.3. The distribution of sodium precursor fragments is shown in Figure 6.4; the peak at $N^*=20$ corresponds to one proton removal in the fast reaction step. However, there is significant contribution from $N^*=18,19$ as well. The production of a wide range of precursor fragments within a given element, seen in Figure 6.4, is not supported by the data.

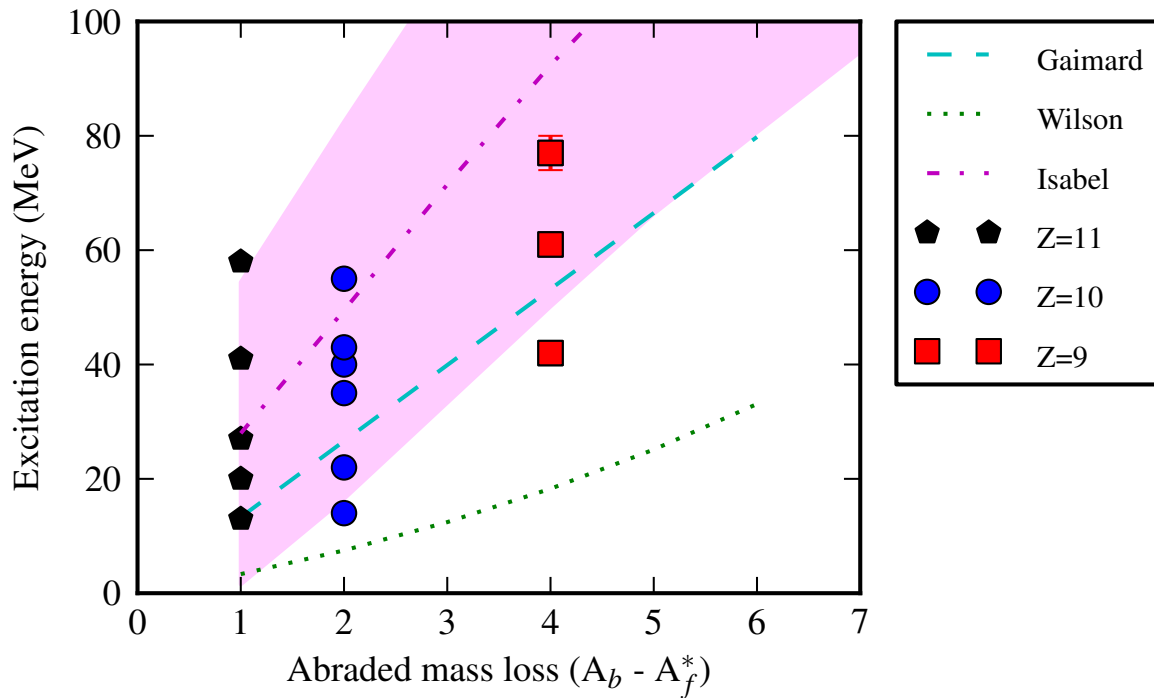


Figure 6.1: Excitation energy (E^*) versus mass loss in the fast reaction step ($A_b - A_f^*$). Two abrasion/ablation models are shown: Wilson [24] and Gaimard [25]. An internuclear cascade model is also shown, ISABEL [26], [27]. The line represents the average excitation energy produced in the simulation for a precursor fragment with charge $Z=11$. The bounds of the ISABEL region give the RMS for the excitation energy distribution for a given mass loss, again for $Z=11$. The trends are similar for lower charges.

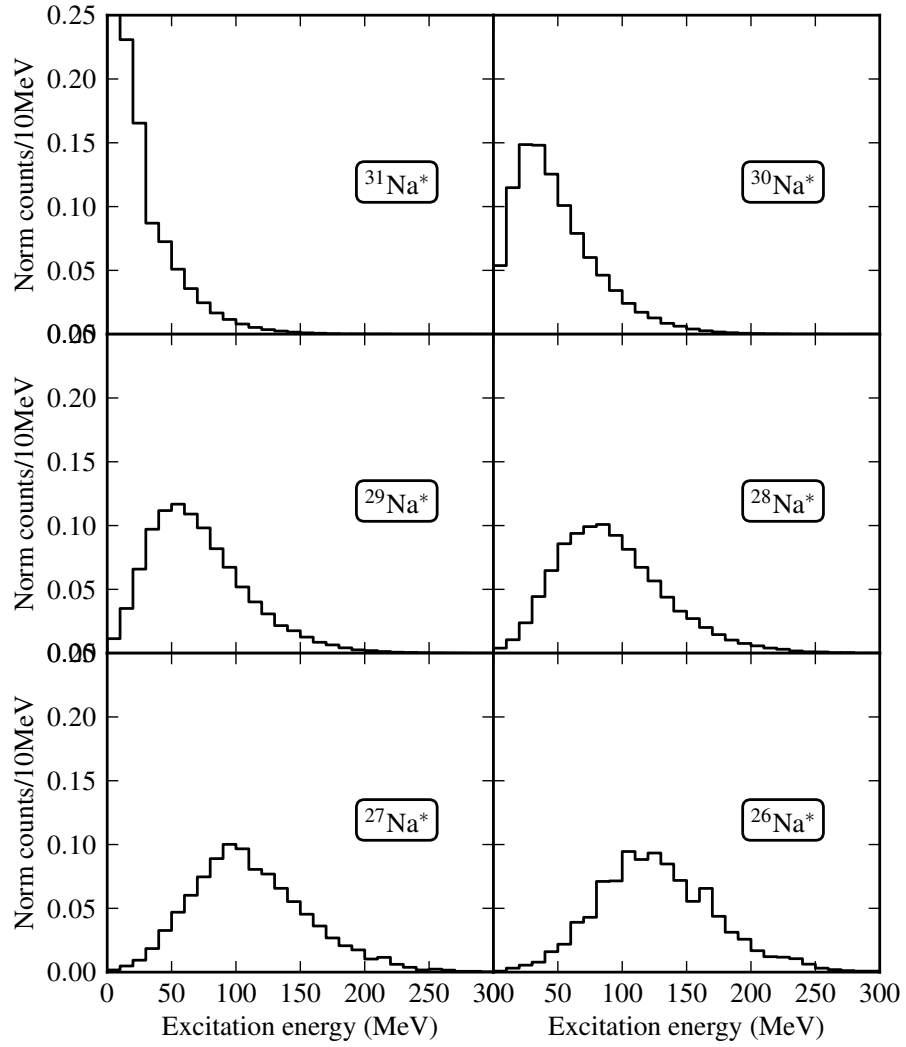


Figure 6.2: Excitation energy (E^*) distributions for $Z=11$ (Na) precursor fragments from the ISABEL model of the present reaction ($^{32}\text{Mg} + ^9\text{Be}$). Sodium fragments are shown to illustrate a fast-step mass loss of one.

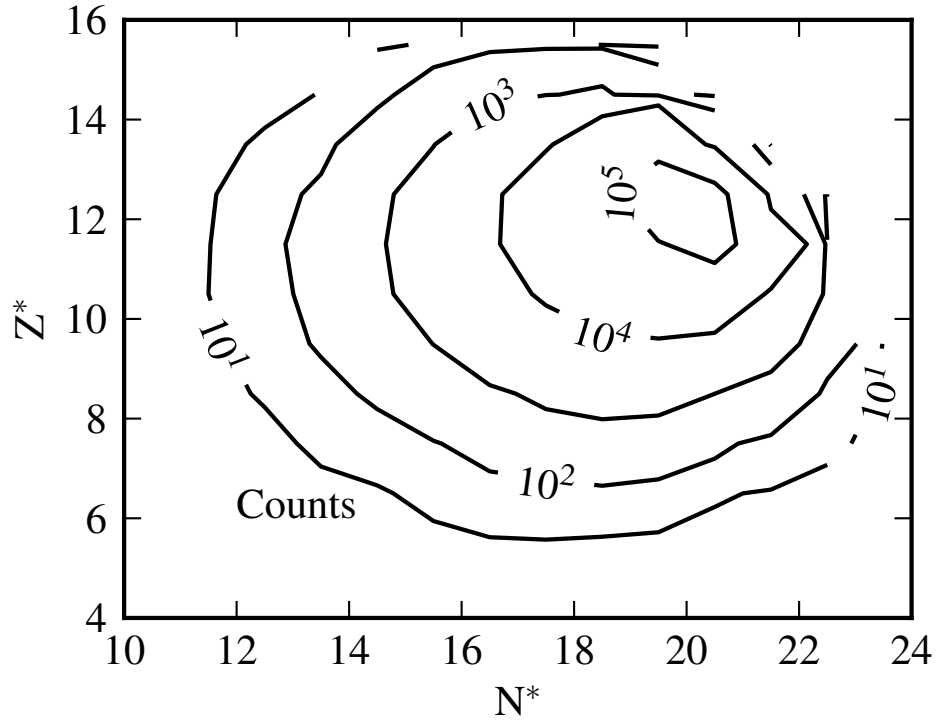


Figure 6.3: Contours of the relative production cross section for precursor fragments from the ISABEL model of the reaction of ^{32}Mg with ^9Be .

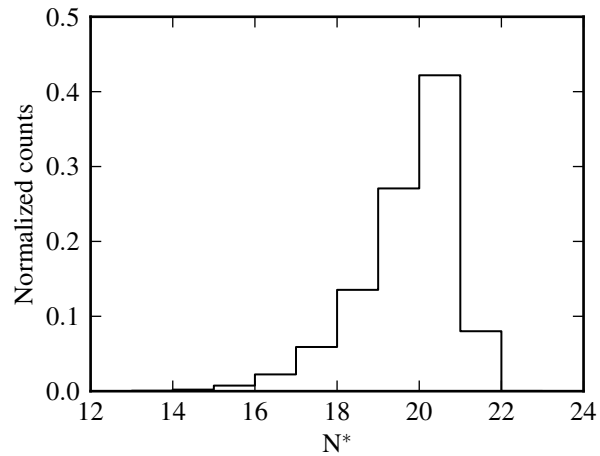


Figure 6.4: Normalized production cross section for sodium ($Z^*=11$) precursor fragments from the ISABEL model of the reaction of ^{32}Mg with ^9Be .

Chapter 7

CONCLUSIONS

The projectile fragmentation mechanism was studied through the detection of evaporated neutrons in coincidence with charged projectile fragments. The experiment was conducted at NSCL, where a ^{48}Ca primary beam was used to produce a ^{32}Mg secondary beam at 86 MeV/u, which was selected from contaminants using the A1900 fragment separator. The beam was then transported to the N2 vault, where a beryllium reaction target was used in a second projectile fragmentation reaction. The charged fragments produced in this secondary target were bent away from zero degrees using the Sweeper magnet and identified using an array of detectors in the focal plane, while any forward-emitted neutrons continued unobstructed to MoNA/MoNA' where they were detected and correlated to the charged fragments on an event-by-event basis.

The resultant neutron hit multiplicity from MoNA/MoNA' was compared to results of a statistical evaporation calculation (PACE), which was passed through a GEANT4 simulation to account for the detector response. Based on the χ^2_{ν} curves from this simulation, a best precursor fragment mass and excitation energy were determined for each fragment detected in the Sweeper focal plane. These results were compared to microscopic and macroscopic excitation models within the abrasion/ablation framework and to an internuclear cascade model.

All observed fragments showed an increase in excitation energy with total mass loss ($A_b - A_f$). The sodium and neon fragments showed a single best precursor mass ($A=31$ and $A=30$, respectively) with a wide range of excitation energies that increased as a function of total mass loss for the final fragment. The fluorine isotopes still showed a wide range of excitation energies, though there is some variation in the precursor mass.

This wide range of excitation energies and small mass loss is not consistent with the

abrasion/ablation model, where the geometric picture leads to a linear increase in excitation energy with abrasion mass loss, $A_b - A_f^*$, and a narrow range of produced excitation energies. The excitation energies obtained in this work are higher in value than those predicted by either a macroscopic or microscopic view of the excitation energy in the abrasion/ablation model and vary widely for a single $A_b - A_f^*$. The internuclear cascade model does give a wide range in excitation energy for fragments, which is supported by the result. However, the wide range of precursor fragments predicted by the internuclear cascade model is not consistent with the results of this experiment. The data suggest that a wide range of fragments of a given element were produced from a single precursor mass.

The lack of consistency between the results of the present experiment and both the abrasion/ablation and internuclear cascade models, indicates that the mechanism for generation of excitation energy in projectile fragmentation reactions is not well understood. Further experiments to determine the precursor mass over a wider mass region are needed to constrain the reaction mechanism. Results from a much heavier system would be particularly informative, as a large number of isotopic chains in a wide range of elements could be studied with the same experimental uncertainties.

BIBLIOGRAPHY

BIBLIOGRAPHY

- [1] D. J. Morrissey, B. M. Sherrill, M. Steiner, A. Stolz, and I. Wiedenhoever, “Commissioning the a1900 projectile fragment separator,” *Nuclear Instruments and Methods in Physics Research Section B: Beam Interactions with Materials and Atoms*, vol. 204, pp. 90 – 96, 2003. 14th International Conference on Electromagnetic Isotope Separators and Techniques Related to their Applications.
- [2] M. Mocko, M. B. Tsang, L. Andronenko, M. Andronenko, F. Delaunay, M. Famiano, T. Ginter, V. Henzl, D. Henzlová, H. Hua, S. Lukyanov, W. G. Lynch, A. M. Rogers, M. Steiner, A. Stolz, O. Tarasov, M.-J. v. Goethem, G. Verde, W. S. Wallace, and A. Zallesov, “Projectile fragmentation of ^{40}Ca , ^{48}Ca , ^{58}Ni , and ^{64}Ni at 140 mev/nucleon,” *Phys. Rev. C*, vol. 74, p. 054612, Nov 2006.
- [3] G. A. Souliotis, R. Harkewicz, K. N. McDonald, D. J. Morrissey, Y. Chen, E. Kashy, B. M. Sherrill, N. A. Orr, and J. A. Winger, “Differential cross sections of projectilelike fragments from ^{18}O and ^{40}Ar at $E / A = 80$ mev,” *Phys. Rev. C*, vol. 49, pp. 3301–3304, Jun 1994.
- [4] M. Mocko, M. B. Tsang, Z. Y. Sun, N. Aoi, J. M. Cook, F. Delaunay, M. A. Famiano, H. Hui, N. Imai, H. Iwasaki, W. G. Lynch, T. Motobayashi, M. Niikura, T. Onishi, A. M. Rogers, H. Sakurai, A. Stolz, H. Suzuki, E. Takeshita, S. Takeuchi, and M. S. Wallace, “Projectile fragmentation of ^{86}Kr at 64 mev/nucleon,” *Phys. Rev. C*, vol. 76, p. 014609, Jul 2007.
- [5] M. Notani, H. Sakurai, N. Aoi, H. Iwasaki, N. Fukuda, Z. Liu, K. Yoneda, H. Ogawa, T. Teranishi, T. Nakamura, H. Okuno, A. Yoshida, Y. X. Watanabe, S. Momota, N. Inabe, T. Kubo, S. Ito, A. Ozawa, T. Suzuki, I. Tanihata, and M. Ishihara, “Projectile fragmentation reactions and production of nuclei near the neutron drip line,” *Phys. Rev. C*, vol. 76, p. 044605, Oct 2007.
- [6] O. Tarasov and D. Bazin, “Lise++: Radioactive beam production with in-flight separators,” *Nuclear Instruments and Methods in Physics Research Section B: Beam Interactions with Materials and Atoms*, vol. 266, no. 19-20, pp. 4657 – 4664, 2008. Proceedings of the XVth International Conference on Electromagnetic Isotope Separators and Techniques Related to their Applications.
- [7] K. Sümmerer, W. Bröchle, D. J. Morrissey, M. Schädel, B. Szweryn, and Y. Weifan, “Target fragmentation of au and th by 2.6 gev protons,” *Phys. Rev. C*, vol. 42, pp. 2546–2561, Dec 1990.
- [8] <https://intra.nslc.msui.edu/includes/imageDisplay.php?id=972&short=1&long=1>.
- [9] D. J. Morrissey, “Systematics of momentum distributions from reactions with relativistic ions,” *Phys. Rev. C*, vol. 39, pp. 460–470, Feb 1989.

- [10] O. Tarasov, “Analysis of momentum distributions of projectile fragmentation products,” *Nuclear Physics A*, vol. 734, no. 0, pp. 536 – 540, 2004. Proceedings of the Eighth International Conference On Nucleus-Nucleus Collisions.
- [11] K. Van Bibber, D. L. Hendrie, D. K. Scott, H. H. Weiman, L. S. Schroeder, J. V. Geaga, S. A. Cessin, R. Treuhaft, Y. J. Grossiord, J. O. Rasmussen, and C. Y. Wong, “Evidence for orbital dispersion in the fragmentation of ^{16}O at 90 and 120 mev/nucleon,” *Phys. Rev. Lett.*, vol. 43, pp. 840–844, Sep 1979.
- [12] D. E. Greiner, P. J. Lindstrom, H. H. Heckman, B. Cork, and F. S. Bieser, “Momentum distributions of isotopes produced by fragmentation of relativistic ^{12}C and ^{16}O projectiles,” *Phys. Rev. Lett.*, vol. 35, pp. 152–155, Jul 1975.
- [13] A. S. Goldhaber and H. H. Heckman, “High energy interactions of nuclei,” *Annual Review of Nuclear and Particle Science*, vol. 28, no. 1, pp. 161–205, 1978.
- [14] J. Bowman, W. Swiatecki, and C. Tsang, “Abrasion and ablation of heavy ions,” 1973-07-01.
- [15] T. Baumann, J. Boike, J. Brown, M. Bullinger, J. Bychoswki, S. Clark, K. Daum, P. DeYoung, J. Evans, J. Finck, N. Frank, A. Grant, J. Hinnefeld, G. Hitt, R. Howes, B. Isselhardt, K. Kemper, J. Longacre, Y. Lu, B. Luther, S. Marley, D. McCollum, E. McDonald, U. Onwuemene, P. Pancella, G. Peaslee, W. Peters, M. Rajabali, J. Robertson, W. Rogers, S. Tabor, M. Thoennessen, E. Tryggestad, R. Turner, P. VanWylen, and N. Walker, “Construction of a modular large-area neutron detector for the nscl,” *Nuclear Instruments and Methods in Physics Research Section A: Accelerators, Spectrometers, Detectors and Associated Equipment*, vol. 543, no. 2-3, pp. 517 – 527, 2005.
- [16] M. Bird, S. Kenney, J. Toth, H. Weijers, J. DeKamp, M. Thoennessen, and A. Zeller, “System testing and installation of the nhmfl/nscl sweeper magnet,” *IEEE Transactions on Applied Superconductivity*, vol. 15, pp. 1252 – 1254, 2005.
- [17] A. Gavron, “Statistical model calculations in heavy ion reactions,” *Phys. Rev. C*, vol. 21, pp. 230–236, Jan 1980.
- [18] K. Chen, Z. Fraenkel, G. Friedlander, J. R. Grover, J. M. Miller, and Y. Shimamoto, “Vegas: A monte carlo simulation of intranuclear cascades,” *Phys. Rev.*, vol. 166, pp. 949–967, Feb 1968.
- [19] D. J. Morrissey, L. F. Oliveira, J. O. Rasmussen, G. T. Seaborg, Y. Yariv, and Z. Fraenkel, “Microscopic and macroscopic model calculations of relativistic heavy-ion fragmentation reactions,” *Phys. Rev. Lett.*, vol. 43, pp. 1139–1142, Oct 1979.
- [20] T. Shibata, H. Ejiri, J. Chiba, S. Nagamiya, K. Nakai, R. Anholt, H. Bowman, J. Ingersoll, E. Rauscher, and J. Rasmussen, “In-beam nuclear gamma-ray studies of relativistic heavy ion reactions,” *Nuclear Physics A*, vol. 308, no. 3, pp. 513 – 531, 1978.

- [21] J. Gosset, H. H. Gutbrod, W. G. Meyer, A. M. Poskanzer, A. Sandoval, R. Stock, and G. D. Westfall, “Central collisions of relativistic heavy ions,” *Phys. Rev. C*, vol. 16, pp. 629–657, Aug 1977.
- [22] D. J. Morrissey, W. R. Marsh, R. J. Otto, W. Loveland, and G. T. Seaborg, “Target residue mass and charge distributions in relativistic heavy ion reactions,” *Phys. Rev. C*, vol. 18, pp. 1267–1274, Sep 1978.
- [23] L. F. Oliveira, R. Donangelo, and J. O. Rasmussen, “Abrasion-ablation calculations of large fragment yields from relativistic heavy ion reactions,” *Phys. Rev. C*, vol. 19, pp. 826–833, Mar 1979.
- [24] J. W. Wilson, L. W. Townsend, and F. Badavi, “A semiempirical nuclear fragmentation model,” *Nuclear Instruments and Methods in Physics Research Section B: Beam Interactions with Materials and Atoms*, vol. 18, no. 1-6, pp. 225 – 231, 1986.
- [25] J. J. Gaimard and K. H. Schmidt, “A reexamination of the abrasion-ablation model for the description of the nuclear fragmentation reaction,” *Nuclear Physics A*, vol. 531, no. 3-4, pp. 709 – 745, 1991.
- [26] Y. Yariv and Z. Fraenkel, “Intranuclear cascade calculation of high-energy heavy-ion interactions,” *Phys. Rev. C*, vol. 20, pp. 2227–2243, Dec 1979.
- [27] Y. Yariv and Z. Fraenkel, “Intranuclear cascade calculation of high energy heavy ion collisions: Effect of interactions between cascade particles,” *Phys. Rev. C*, vol. 24, pp. 488–494, Aug 1981.
- [28] G. S. W. Loveland, D.J. Morrissey, *Modern Nuclear Chemistry*. John Wiley & Sons, 2006.
- [29] A. Gilbert and A. G. W. Cameron, “A composite nuclear-level density formula with shell corrections,” *Canadian Journal of Physics*, vol. 43, no. 8, pp. 1446–1496, 1965.
- [30] O. Tarasov and D. Bazin, “Development of the program lise: application to fusion evaporation,” *Nuclear Instruments and Methods in Physics Research Section B: Beam Interactions with Materials and Atoms*, vol. 204, no. 0, pp. 174 – 178, 2003. 14th International Conference on Electromagnetic Isotope Separators and Techniques Related to their Applications.
- [31] K.-H. Schmidt, M. Ricciardi, A. Botvina, and T. Enqvist, “Production of neutron-rich heavy residues and the freeze-out temperature in the fragmentation of relativistic ^{238}U projectiles determined by the isospin thermometer,” *Nuclear Physics A*, vol. 710, no. 1-2, pp. 157 – 179, 2002.
- [32] T. Enqvist, J. Benlliure, F. Farget, K.-H. Schmidt, P. Armbruster, M. Bernas, L. Tassan-Got, A. Boudard, R. Legrain, C. Volant, C. BÄückstiegel, M. de Jong, and J. Dufour, “Systematic experimental survey on projectile fragmentation and fission induced in collisions of ^{238}U at 1 a gev with lead,” *Nuclear Physics A*, vol. 658, no. 1, pp. 47 – 66, 1999.

- [33] C. Freigang, “Building the sweeper magnet focal plane detector,” Master’s thesis, Michigan State University, 2001.
- [34] G. F. Knoll, *Radiation Detection and Measurement*. John Wiley & Sons, Inc., 2000.
- [35] W. Peters, *Study of Neutron Unbound States Using the Modular Neutron Array (MoNA)*. PhD thesis, Michigan State University, 2007.
- [36] N. Frank, *Spectroscopy of Neutron Unbound States in the Neutron Rich Oxygen Isotopes*. PhD thesis, Michigan State University, 2006.
- [37] C. Hoffman, *Investigation of the Neutron-rich Oxygen Isotopes at the Drip Line*. PhD thesis, Florida State University, 2009.
- [38] P. Bhattacharjee and G. Sigl, “Origin and propagation of extremely high-energy cosmic rays,” *Physics Reports*, vol. 327, no. 3-4, pp. 109 – 247, 2000.
- [39] “Milagro gamma-ray observatory.” <http://www.lanl.gov/milagro/cosmicrays.shtml>.
- [40] G. A. Christian, *Spectroscopy of neutron-unbound fluorines*. PhD thesis, Michigan State University, 2011.
- [41] S. Agostinelli, J. Allison, K. Amako, J. Apostolakis, H. Araujo, P. Arce, M. Asai, D. Axen, S. Banerjee, G. Barrand, F. Behner, L. Bellagamba, J. Boudreau, L. Broglia, A. Brunengo, H. Burkhardt, S. Chauvie, J. Chuma, R. Chytracsek, G. Cooperman, G. Cosmo, P. Degtyarenko, A. Dell’Acqua, G. Depaola, D. Dietrich, R. Enami, A. Feliciello, C. Ferguson, H. Fesefeldt, G. Folger, F. Foppiano, A. Forti, S. Garelli, S. Giani, R. Giannitrapani, D. Gibin, J. J. G. Cadenas, I. González, G. G. Abril, G. Greeniaus, W. Greiner, V. Grichine, A. Grossheim, S. Guatelli, P. Gumplinger, R. Hamatsu, K. Hashimoto, H. Hasui, A. Heikkinen, A. Howard, V. Ivanchenko, A. Johnson, F. W. Jones, J. Kallenbach, N. Kanaya, M. Kawabata, Y. Kawabata, M. Kawaguti, S. Kelner, P. Kent, A. Kimura, T. Kodama, R. Kokoulin, M. Kossov, H. Kurashige, E. Lamanna, T. Lampén, V. Lara, V. Lefebure, F. Lei, M. Liendl, W. Lockman, F. Longo, S. Magni, M. Maire, E. Medernach, K. Minamimoto, P. M. de Freitas, Y. Morita, K. Murakami, M. Nagamatu, R. Nartallo, P. Nieminen, T. Nishimura, K. Ohtsubo, M. Okamura, S. O’Neale, Y. Oohata, K. Paech, J. Perl, A. Pfeiffer, M. G. Pia, F. Ranjard, A. Rybin, S. Sadilov, E. D. Salvo, G. Santin, T. Sasaki, N. Savvas, Y. Sawada, S. Scherer, S. Sei, V. Sirotenko, D. Smith, N. Starkov, H. Stoecker, J. Sulkimo, M. Takahata, S. Tanaka, E. Tcherniaev, E. S. Tehrani, M. Tropeano, P. Truscott, H. Uno, L. Urban, P. Urban, M. Verderi, A. Walkden, W. Wander, H. Weber, J. P. Wellisch, T. Wenaus, D. C. Williams, D. Wright, T. Yamada, H. Yoshida, and D. Zschesche, “G4—a simulation toolkit,” *Nuclear Instruments and Methods in Physics Research Section A: Accelerators, Spectrometers, Detectors and Associated Equipment*, vol. 506, no. 3, pp. 250 – 303, 2003.
- [42] P. Desesquelles, A. Cole, A. Dauchy, A. Giorni, D. Heuer, A. Lleres, C. Morand, J. Saint-Martin, P. Stassi, J. Viano, B. Chambon, B. Cheynis, D. Drain, and C. Pastor, “Cross talk and diaphony in neutron detectors,” *Nuclear Instruments and Methods in Physics*

Research Section A: Accelerators, Spectrometers, Detectors and Associated Equipment,
vol. 307, no. 2-3, pp. 366 – 373, 1991.

- [43] “Endf.vii.” <http://www-nds.iaea.org/exfor/endl.htm>.
- [44] Z. Kohley Private communication, September 2011.
- [45] “Numerical recipes.” <http://library.lanl.gov/numerical>.